

Article

Oxide Strontium-Barium Perovskites Ceramics: Examinations of Structural Phase Transitions and Potential Application as Oxygen Carriers

Ewelina Ksepko ^{*}, Rafal Lysowski and Miratul Alifah

Department of Engineering and Technology of Chemical Processes, Wrocław University of Science and Technology, 7/9 Gdanska, 50-373 Wrocław, Poland

^{*} Correspondence: ewelina.ksepko@pwr.edu.pl; Tel.: +48-71-320-65-321

Abstract: The structural properties of selected $(\text{Ba}_{1-x}\text{Sr}_x)\text{PbO}_3$ ceramics were examined at 14–1148 K using X-ray powder diffraction (XRD). These materials are attractive due to their variety of applications, such as, for example, high-temperature thermoelectric energy conversion. Attention was paid to this paper as a continuation of the previous examinations of higher Sr^{2+} concentrations. The type of perovskite distortion and temperatures of the structural phase transitions (SPTs) were determined from the splitting of certain pseudocubic lines. At this point, for example $(\text{Ba}_{0.3}\text{Sr}_{0.7})\text{PbO}_3$ showed three temperature-induced SPTs. When the amount of Sr increased in the samples, no phase transition was observed, which is contrary to the data previously demonstrated in the literature. The quality of the ceramics was examined by scanning electron microscopy-energy dispersion X-ray spectroscopy (SEM-EDS), demonstrating their homogeneity and uniform elements dispersion. As a result of profound crystal investigations, confirmed by thermogravimetric analysis and quadrupole mass spectroscopy (TGA-QMS), a phase diagram was prepared for the $(\text{Ba}_{1-x}\text{Sr}_x)\text{PbO}_3$ system based on our former and recent study. Also, the investigation of a new application for the $(\text{Ba}_{1-x}\text{Sr}_x)\text{PbO}_3$ family is presented in this paper for the first time. The TGA analysis was conducted on Illinois#6 hard coal to evaluate the capability of perovskites to be used in the chemical looping combustion (CLC) process in a range of temperatures 1073–1173 K. Due to its thermal stability and reactivity, $\text{Ba}_{0.9}\text{Sr}_{0.1}\text{PbO}_3$ is the material with the greatest potential to be applied as an oxygen carrier. The combination of strontium and barium offers encouraging results compared to the pure barium and strontium lead oxide perovskites.

Keywords: ceramics; doped perovskites; X-ray diffraction; phase transitions; oxygen carriers; thermogravimetric analysis



Citation: Ksepko, E.; Lysowski, R.; Alifah, M. Oxide Strontium-Barium Perovskites Ceramics: Examinations of Structural Phase Transitions and Potential Application as Oxygen Carriers. *Processes* **2023**, *11*, 2144. <https://doi.org/10.3390/pr11072144>

Academic Editors: Denis Kuznetsov, Maria Vartanyan and Andrey Yurkov

Received: 25 May 2023
Revised: 7 July 2023
Accepted: 14 July 2023
Published: 18 July 2023



Copyright: © 2023 by the authors. Licensee MDPI, Basel, Switzerland. This article is an open access article distributed under the terms and conditions of the Creative Commons Attribution (CC BY) license (<https://creativecommons.org/licenses/by/4.0/>).

1. Introduction

Today, there is increasing attention towards perovskite-type materials [1–5]. This is mainly due to their excellent properties and practical applications. Many of these materials have interesting properties such as ferroelectricity or ferromagnetism (used as sensors and data storage devices) [6], etc. Furthermore, they are used as supercapacitors for electrochemical energy storage (batteries and electrochemical capacitors) [7–9]. Some have successfully been used as perovskite solar cells (PVSCs) [10–13] due to their remarkable efficiency increase of nearly 24% compared to commercial Si solar cells [1], or ceramic foam membranes for oxygen [2] or carbon dioxide transport [14]. Others have been used as superior perovskite electrocatalysts [15], possessing multiferroic properties together with polarization-induced photoelectrochemical activity, for water splitting applications [16]; and as so-called oxygen carriers in energy-generation processes [17–19] due to the reversible and fast change of oxygen content for many cycles at high temperatures. When external conditions such as temperature or pressure are used, changes in their physical or structural properties are observed [12,20]. The perovskite structure is most commonly found for

compounds with a general ABX_3 formula. An A is commonly a metal with a +1 or +2 oxidation state, B is a metal with a +3, +4, or +5 oxidation state, while an X is an anion, most often an oxide or fluoride.

Research into changes in the structure and physical properties of perovskites are relevant for their further industrial application. Doping perovskites with certain metals could alter their structure; also, the admixture of certain materials can improve their stability under certain conditions, such as high temperatures, preventing unfavorable changes in structure, which could be important if the material is applied to work in a wide range of temperatures. Proper composition allows the material to maintain its properties in such an environment [21–23].

Among the interesting examples of perovskites, $(Ba_{1-x}Sr_x)PbO_3$ compounds can be highlighted. The reason for this is their variety of applications, such as high-temperature thermoelectric energy conversion, as reported in [7,9,24–26]. Furthermore, they may be applied to prevent the corrosion of long-life batteries, which are usually coated with oxide layers of $SrPbO_3$ [27].

Shannon et al. [28] reported an orthorhombic $Pbnm$ symmetry for $SrPbO_3$ ceramic, while Keeler et al. [29] analyzed the observed $Pnma$ space group of $SrPbO_3$ monocrystals with $a = 5.964 \text{ \AA}$, $b = 8.320 \text{ \AA}$, $c = 5.860 \text{ \AA}$. Furthermore, Fu and Ido proposed re-examining its structure in response to Ritter's paper [30]. They applied the powder neutron diffraction technique and estimated the tilt angles of the octahedra tilting in the $[110]_c$ and $[001]_c$ directions as 15.1° and 11° , which was noted as $a^-a^-c^+$. Then, Shuvaeva et al. [31] for $SrPbO_3$ at 298 K reported a monoclinic distortion of perovskite cells with the following pseudocubic cell parameters: $a_c = c_c = 4.17 (6) \text{ \AA}$, $b_c = 4.16 (6) \text{ \AA}$, $\beta = 90^\circ 53'$. There is a good agreement on the crystal structure of $SrPbO_3$ ($Pnma$, or $Pbnm$) at room temperature, even when different techniques are applied [29,32–35].

Only partial information is available for $SrPbO_3$ -doped materials, such as $(Ba_{0.8}Sr_{0.2})PbO_3$ and $(Ba_{0.3}Sr_{0.7})PbO_3$ ceramics. An assumed symmetry of $Imma$ is reported as well as pure $BaPbO_3$ [32,36]. Moreover, a high-temperature behavior study for undoped $SrPbO_3$ showed very different results. For example, in paper [29], the transition from the orthorhombic to the cubic phase was observed at about 1123 K. In another paper [35], a tetragonal phase transition was observed at 723 K. Based on the splitting of the main diffraction line of the $\{211\}$ type, the authors also suggested a possible cubic phase transition close to 1023 K. However, they did not observe it during the examinations. Therefore, Hester et al. [32] investigated the crystalline structure of the $SrPbO_3$ compound by X-ray diffraction in the 298–1033 K range. He was skeptical of the report of Keester et al. [37]. The obtained results showed that in the studied high-temperature range, the observed symmetry was $Pnma$. He suggested that if a structural transition was present, it would be $Pnma-Imma$, due to the change in the type of PbO_6 octahedral tilting from $a^+b^-b^-$ to $a^0b^-b^-$. Moreover, only a few works have been published on the study of crystalline structure at low temperatures, but they only concern the $BaPbO_3$ perovskite [38,39].

The literature on related perovskite series $(Ba_{1-x}Sr_x)PbO_3$ is limited. Principally, this is because the reports discuss the application of pure $SrPbO_3$ and $BaPbO_3$ and their crystal structure. There is no information on the crystalline structure of the mixed $(Ba_{1-x}Sr_x)PbO_3$ compounds, both at room temperature and at low and high temperatures. Therefore, it is necessary to precisely describe the crystalline structure of compounds based on $SrPbO_3$, where strontium ions are substituted with barium ions.

Understanding where physicochemical values like material composition, temperature or pressure, and certain phase transitions overlap is helpful for developing more stable materials that are able to work under a broader range of physical conditions, which is particularly important in applications like solar energy devices, sensors [22], or high-temperature solid oxide fuel cells [40,41]. In view of the uncertainties in the published data, a redetermination of the phases of $(Ba_{1-x}Sr_x)PbO_3$ was carried out.

The aim of this work is to determine both the crystalline structure at RT and evaluate the potential structural phase transitions of $(Ba_{1-x}Sr_x)PbO_3$ ceramics as a function of tem-

perature, from as low as 14 K to 1143 K. Furthermore, the description of the mechanism responsible for the distortions of the observed structures in the examined perovskites is a key issue. In the present work, the powder X-ray diffraction (XRD) method was applied to determine the parameters of the crystalline structure parameters. On this basis, the phase composition, symmetry, distortion, and the potential presence of structural phase transitions were determined. The purity and homogeneity of the obtained ceramics were additionally examined with scanning electron microscopy combined with an energy dispersion X-ray spectrometer (SEM-EDS). To support the observed phenomena, simultaneous thermogravimetry—differential scanning calorimetry (STA/TG-DSC) coupled to a quadrupole mass spectrometer (QMS)—was additionally applied. To test the perovskites' potential application in chemical looping combustion (CLC) processes, a TGA study was also carried out using the Illinois#6 hard coal and the synthesized materials.

2. Materials and Methods

2.1. Synthesis of $(\text{Ba}_{1-x}\text{Sr}_x)\text{PbO}_3$ and the Materials Quality Examination

The research presented in this paper is a natural continuation of the research work of our group on barium-strontium ceramics [20,42]. As a result, the focus here was placed on a higher concentration of strontium in the samples.

Samples of the $(\text{Ba}_{1-x}\text{Sr}_x)\text{PbO}_3$ series were obtained from BaCO_3 , SrCO_3 and PbO_2 powders (>99.9% POCH; Sigma Aldrich, St. Louis, MO, USA). Stoichiometric amounts of the starting materials were thoroughly ground and pelletized ($15 \times 5 \times 5$ mm at 20 MPa) and then heated in flowing air at 1073 K for 20 h. The pellets were then reground, remixed, re-pelleted, and heated again in the air at 1223 K for 15 min. The resulting material was ground and sieved. The optimal calcination conditions were selected based on pre-testing. The formation of perovskite compounds was confirmed by X-ray diffraction [20,42].

The microstructure of the material surface was studied using scanning electron microscopy by means of a JEOL JSM—6610 LV (Tokyo, Japan) instrument with an energy dispersion X-ray spectrometer for chemical microanalysis purposes. The surface morphology was studied by gluing carbon tape onto the samples; carbon tape was not used in the chemical analysis of the samples. The study was carried out using a low vacuum detector at an accelerating voltage of 15 kV and different magnifications of the image (50–1500 \times). EDS with a Si(Li) X-ray detector (Oxford Instruments, Abingdon, UK) was used to investigate the homogeneity of the samples. Microphotographs, of a 250 \times magnification of $(\text{Ba}_{1-x}\text{Sr}_x)\text{PbO}_3$ perovskites powders, are shown in Figure 1. The ceramic powders were fine and dense, with a grain size estimated at 15 microns for those with Sr^{2+} concentrations from 0.5 to 1. For concentrations of $x \leq 0.5$, some bigger grain sizes, ca. 50 microns, were observed. The composition analysis by EDS showed no presence of impurities in the final ceramics, for example, as seen in Figure 2. The mapping analysis carried out proved that the obtained samples were homogeneous with a uniform distribution of atoms. An example of SrPbO_3 mapping specifically for Sr, Pb, and O elements is shown in Figure 2b.

The perovskite crystals belong to a group of ionic compounds. The structure of the ideal perovskite with the general formulae of ABX_3 is a regular cell with the atoms occupying specific positions, which are A^+ : 000, B^+ : $\frac{1}{2} \frac{1}{2} \frac{1}{2}$, and X^- : $\frac{1}{2} \frac{1}{2} 0$, $\frac{1}{2} 0 \frac{1}{2}$, $0 \frac{1}{2} \frac{1}{2}$. For the prediction of the formability of the perovskite structure and its stability, a tolerance factor (τ) was calculated according to the procedure shown elsewhere [13]. For calculating the Goldschmidt factors for $(\text{Ba}_{1-x}\text{Sr}_x)\text{PbO}_3$ ionic radii, $R_{\text{Sr}^{2+}} = 1.44 \text{ \AA}$, $R_{\text{Ba}^{2+}} = 1.61 \text{ \AA}$, $R_{\text{Pb}^{4+}} = 0.775 \text{ \AA}$, $R_{\text{O}^{2-}} = 1.35 \text{ \AA}$ were applied. If this factor is equal to unity, it means that all ions touch each other, and this perovskite is called an ideal. In such a perovskite, usually no structural phase transitions are observed. It is also identified that the crystalline structure is stable when the factor is in the range of values: $0.8 < \tau < 1.0$. The estimated value of the tolerance factor for SrPbO_3 is 0.928, and when some Ba ions are introduced to the lattice—for example for $(\text{Ba}_{0.2}\text{Sr}_{0.8})\text{PbO}_3$ and $(\text{Ba}_{0.3}\text{Sr}_{0.7})\text{PbO}_3$ —it increases to 0.940 and 0.945, respectively. Therefore, from a geometric point of view, stable performance at high temperatures is expected.

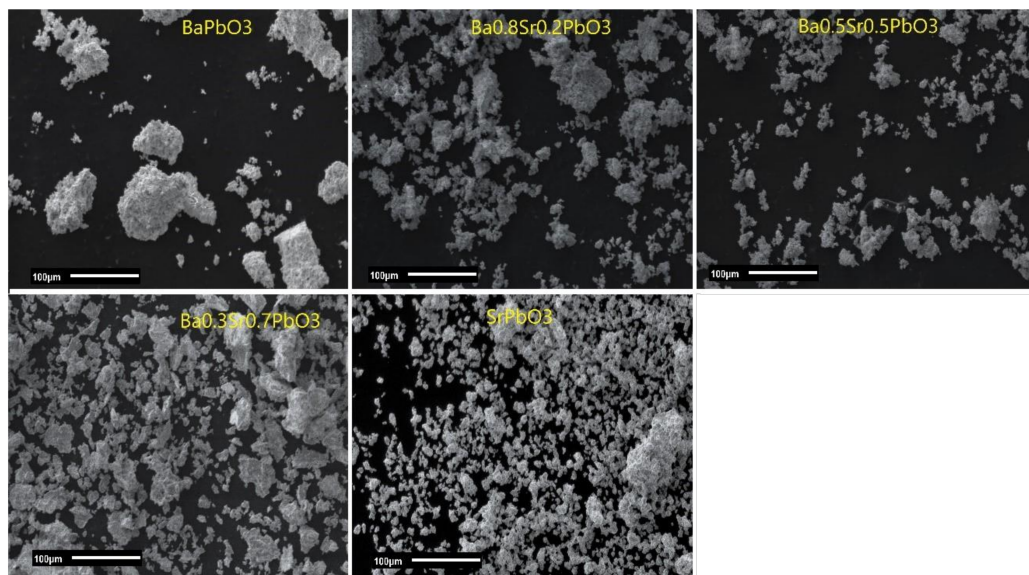


Figure 1. SEM images of $(\text{Ba}_{1-x}\text{Sr}_x)\text{PbO}_3$ series surface at $250\times$ magnification.

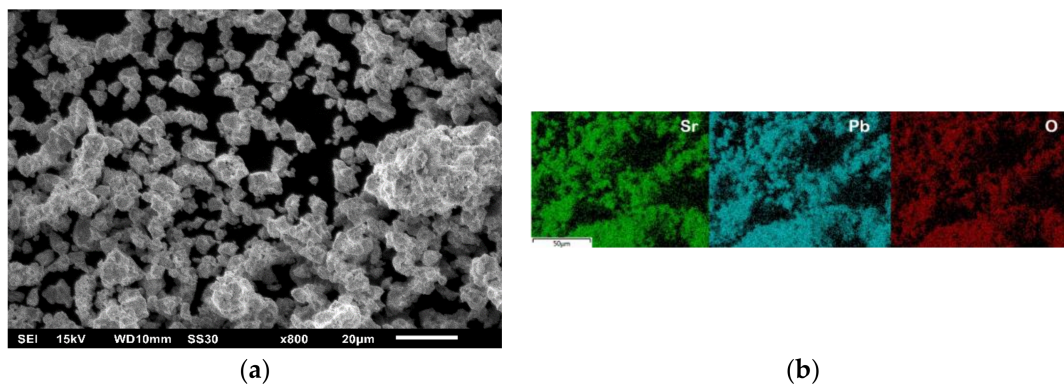


Figure 2. SEM image of SrPbO_3 powders registered at $800\times$ magnification (a), example of distribution maps of Sr, Pb and O ions (b).

2.2. X-ray Diffraction (XRD) Analysis

The phase identification and determination of cell parameters of selected $(\text{Ba}_{1-x}\text{Sr}_x)\text{PbO}_3$ samples were performed using a Siemens D5000 X-ray powder diffractometer (Munich, Germany), with Bragg–Brentano geometry (θ – θ), 40 kV, 25 mA, filtered $\text{CuK}\alpha$ radiation of $\lambda = 1.54056 \text{ \AA}$, a step of 0.02° , 10 s per step, 2θ from 10 to 150° , and a temperature from 14 to $1148 \text{ K} \pm 1 \text{ K}$. Because of the construction of the X-ray diffractometer, the data were collected in the high-temperature range from 298 K to 1148 K and below room temperature from 298 K to 14 K using high-resolution cameras HTK 1200 and He TTK, respectively (Anton Paar, Graz, Austria). Selected pseudocubic lines were measured with 20 and 25 K steps at low and high temperatures, respectively. The analyzed lines contained pseudocubic lines $\{200\}_c$, $\{110\}_c$, $\{220\}_c$, $\{310\}_c$ and $\{222\}_c$. Apart from the main diffraction lines, the superstructure lines were analyzed. The X-ray Powder Reflection Profiler (XP, Poland) program was used for splitting the overlapping diffraction lines and determining their intensity and position. These data were useful for the calculation of the cell parameters for each temperature by the application of the Checkcell program. For Rietveld analysis, the FullProf program was used, which enables structure profile refinement for selected temperatures. Chemical phase analysis was carried out using the International Data for Diffraction Data (JCPDS-ICDD) database. In addition, the crystallite size was determined using a RIGAKU MiniFlex600 powder X-ray powder diffractometer MiniFlex600 by RIGAKU (Tokyo, Japan). Experiments were carried out at 40 kV, 15 mA, filtered $\text{CuK}\alpha$ radiation of $\lambda = 1.54056 \text{ \AA}$, a step of 0.02° ,

5 s per step, for 2θ range from 20 to 90°. The medium crystallite size was determined from about 20 reflections using a pseudo-Voigt profile. The estimated crystallite size varied for samples between 552 Å and 440 Å for undoped SrPbO₃ and BaPbO₃, respectively. As a result of ion substitution, an increase in crystallite size was observed—for example, the (Ba_{0.9}Sr_{0.1})PbO₃ material reached 467 Å.

2.3. Thermogravimetric Analysis (TGA)

Additional testing was aimed at supporting the XRD data. As a result, in this work, simultaneous thermogravimetry—differential scanning calorimetry, STA/TG–DSC, specifically using STA 449 F5 Jupiter apparatus by Netzsch (Selb, Germany)—was applied. In the experiments, the mass changes of the powdered strontium-barium-based perovskites were measured dynamically as a function of time and temperature. A circa 5 mg perovskite sample was placed in an alumina crucible and heated in a synthetic air atmosphere with a heating rate of 15 K/min, with a 25 mL/min flow rate. The sample was treated this way up to 1173 K. When a temperature of 1173 K was reached, the sample was slowly cooled down in oxidizing conditions with a cooling rate of 15 K/min. Mass changes and temperature changes were continuously registered during the experiment. As the STA analyzer cooled down, the samples were collected for post-experiment analysis, i.e., for determining crystal phase changes. In the experiment, working conditions were appropriately tailored by studying the effect of sample mass (5, 20, and 200 mg) and gas flow rates (10–125 mL/min). As a result, final sample masses and used gases rates were set.

Moreover, thermogravimetric experiments for fuel combustion were performed in a thermal analyzer (STA 449 F5 Jupiter (Netzsch, Selb, Germany)), which was paired to a QMS 403C Aeolos (Netzsch, Selb, Germany). The mass spectrometer can detect the mass number of gas in the range 1–300 amu in the MID mode. The analysis was carried out isothermally as a function of a time. The sample was heated from room temperature to requested temperatures (800, 850, and 900 °C; (1073, 1123, and 1173 K) with a heating rate of 20 K/min. The experiments contained two stages: the first was the fuel combustion process and the second was the regeneration of the reduced oxygen carrier with the application of synthetic air, with flow rate of 80 mL/min for 20 min.

For preliminary study, the graphite was chosen as a model fuel. For selected samples of oxide materials, i.e., an SrPbO₃, BaPbO₃, and (Ba_{0.9}Sr_{0.1})PbO₃ analysis of graphite combustion was conducted. The sample weighed in total approximately 100 mg with the 50% surplus of the perovskite and fuel. The samples were placed in an alumina crucible and heated up to the desired process temperatures. The mass changes were analyzed in parallel with the gas analysis. When the process was completed, the samples were collected for the post-analysis. Afterwards, the targeted experiments contained the Illinois#6 hard coal. The Illinois#6 American hard coal was used as combustion fuel in this investigation. The characteristics of the Illinois#6 hard coal [43] are revealed in Table 1.

Table 1. Composition of Illinois#6 hard coal.

Composition	Weight (%)
Moisture	10.40
Ash	9.00
Volatile matter	39.70
Carbon	71.86
Hydrogen	4.93
Nitrogen	1.67
Sulphur	3.77
Oxygen	8.76
Chlorine	0.02

3. Results and Discussion

Below, the comprehensive data on the crystal structure of selected perovskites are included. A detailed study for SrPbO_3 and $(\text{Ba}_{0.2}\text{Sr}_{0.8})\text{PbO}_3$ and $(\text{Ba}_{0.3}\text{Sr}_{0.7})\text{PbO}_3$ is shown as an example, and for other samples, data were included in summarizing figures.

3.1. SrPbO_3 Crystal Structure at Room Temperature (RT)

SrPbO_3 perovskite has received considerable attention in recent decades due to its outstanding properties and applications, as mentioned previously. In this paper, SrPbO_3 crystalline structure evolution was studied with XRD, which was performed over a wide temperature range at both low and high temperatures, i.e., from 14 K to 1148 K. In addition, for the first time, the crystalline structure was studied at low temperatures.

The type of distortion from an ideal cubic perovskite structure was determined using the diffraction lines splitting method and Glazer's analysis, described elsewhere [20]. The pseudocubic distortion was determined, and cell parameters were calculated based on the splitting of the major selected diffraction lines, such as $\{200\}_c$, $\{220\}_c$, $\{222\}_c$. Figure 3 shows the temperature evolutions of $\{220\}_c$ and $\{222\}_c$ reflections for selected 298 K, 723 K, and 1048 K temperatures. Figure 3 shows raw and fit data with $K_{\alpha 1}$ and $K_{\alpha 2}$ lines. Using data from the literature published elsewhere [20], the consideration of the number of main splitting diffraction lines and the analysis of the superstructure lines made it possible to solve the perovskite structure. Therefore, in this paper, the terminology used by Glazer for the classification of space groups and symmetries associated with each of the tilting types is applied. Based on the relationship between the number of major pseudocubic diffraction lines and the given crystallographic system, and the octahedra tilting type for given distortions [44], the distortions and perovskites symmetry were determined.

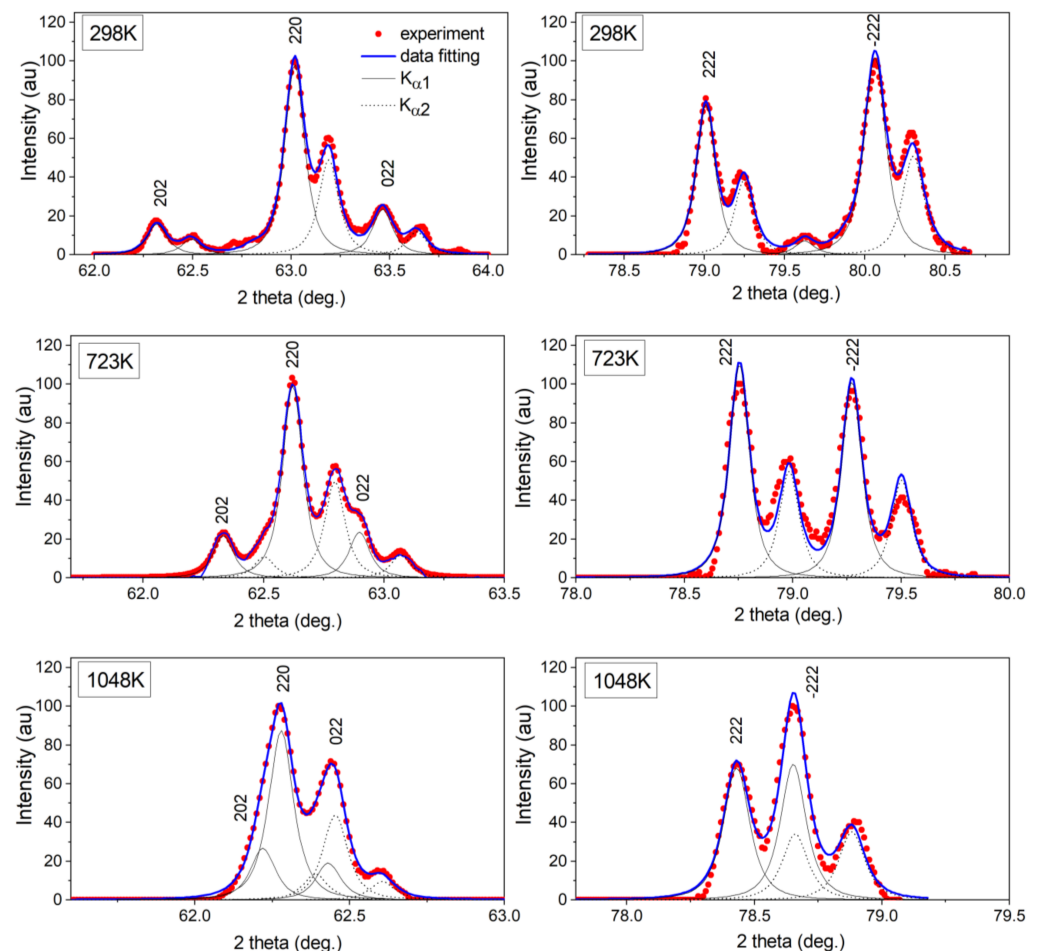


Figure 3. Splitting of the main reflections $\{220\}_c$ and $\{222\}_c$ in the function of temperature for SrPbO_3 .

An analysis of the major diffraction lines at RT indicated the presence of three reflections of the $\{200\}_c$ type, three reflections of $\{220\}_c$, and two of $\{222\}_c$. It can be concluded that the SrPbO_3 pseudocubic cell has three different cell parameters, i.e., $a_c \neq b_c \neq c_c$. Furthermore, based on that information, the expected distortion is monoclinic. Both the intensity and the position of each measured line were fitted using the least-squares method with the application of the X-ray Reflection Profiler program, which further enabled the calculation of cell parameters.

The splitting of the main diffraction lines enabled the determination of the type of unit cell distortion, both at RT and high temperatures. Moreover, additional weak lines with half-Miller indices in the pseudocubic system were observed, as shown in Figure 4. Those lines are called superlattice lines, and the powder pattern data on their observation at RT are collected in Table 1.

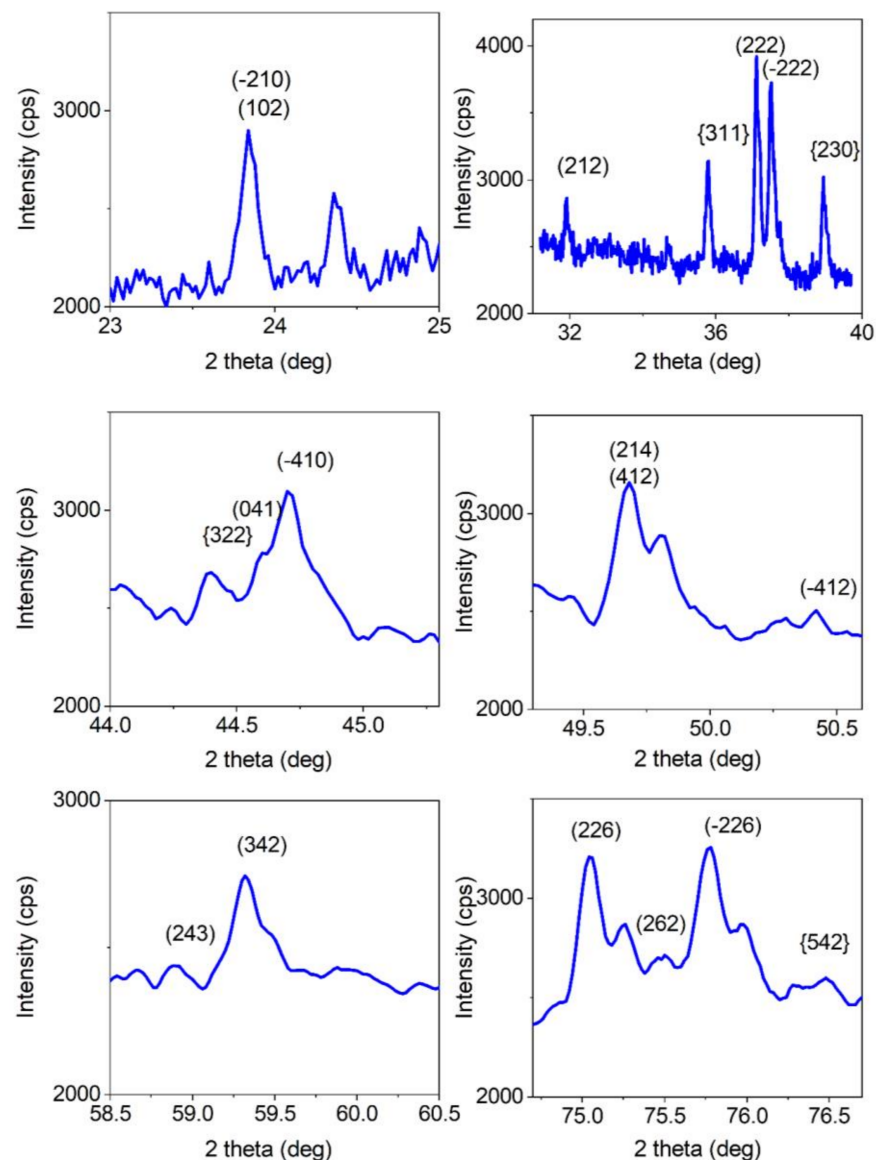


Figure 4. Superstructure lines observed for SrPbO_3 .

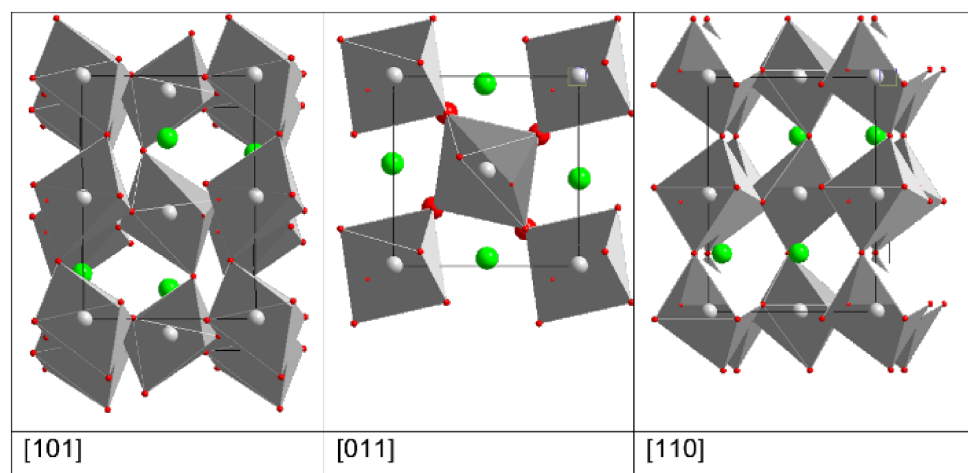
Superlattice lines are obtained as a result of PbO_6 octahedra rotations, called “in phase”, or “out of phase”. Their presence in the XRD pattern indicates if the final cell has a multiplied cell edge, according to Glazer’s theory [44]. The analysis of the superstructure lines showed the presence of both octahedral tilting in the same (+) and in the opposite (−) directions (Table 2).

Table 2. Superstructure line indices and type of PbO_6 octahedra tilting in SrPbO_3 .

Indices in Multiplied Cell (hkl)	Cation Displacement/Octahedra Tilting
302, −302, 320, 322, −322, 124, 142, 502 (odd-even-even)	Sr^{2+} cation displacement from their ideal positions
−311, −131, 311 (odd-odd-odd)	PbO_6 octahedra tilting of a^- type
103, 301, 143, 341, −321, 123, −501, 105 (odd-even-odd)	PbO_6 octahedra tilting of b^+ type

The analysis showed that the monoclinic distortion of the SrPbO_3 structure is caused by both Sr^{2+} cation displacements and by the twisting of the PbO_6 anion octahedra. The indication for this is that some superstructure lines with odd-even-even parity Miller indices, such as (302) or (124), were observed in the X-ray powder pattern (Figure 4). This means that Sr^{2+} cations are shifted from their ideal positions toward the yz direction. However, the presence of (−311) or (113) superstructure lines with odd-odd-odd parity of indices (for $h \neq k$ and $l \neq k$) is a readable proof for PbO_6 octahedra tilting of the a^- type, whereas (143), (−321), (501) with odd-even-odd parity of indices (for $h \neq l$) is of the b^+ type. In other words, the monoclinic distortion is caused by both the rotation of PbO_6 octahedra about the [100] and [010] axes of the primitive cell and by Sr^{2+} cation displacement from their ideal positions. Therefore, two factors have influenced the cell distortion: the cation displacement and octahedra rotation. For that reason, for SrPbO_3 ceramics, the $a^-b^+a^-$ notation can be applied. Those two factors and the observed $a_c \approx c_c \neq b_c$ parameter values lead to assigning them to the $Pbnm$ group. As a result, the monoclinic distortion described by $P2_1/m$ with an orthorhombic symmetry described by the $Pbnm$ space group can be applied for the SrPbO_3 perovskite.

The visualization of the described distortion of the ideal cubic perovskite cell for the SrPbO_3 compound is shown in Figure 5. The crystal structure data for the sample at 298 K are shown in Table 3. From the analysis of Figure 5, rotations of oxygen octahedral are visible in three directions.

**Figure 5.** SrPbO_3 cell with $Pbnm$ orthorhombic symmetry at 298 K. Projections on [101], [011], and [110] planes are shown. Red spheres—oxygen, grey spheres—lead, green spheres—strontium.

To exactly describe the crystalline structure of SrPbO_3 at RT, the ceramic sample was subjected to XRD testing in the $10\text{--}150^\circ$ 2θ range. The structural evolution of SrPbO_3 was analyzed using the Rietveld method. As a result, Figure 6 shows the powder diffractogram for SrPbO_3 obtained at room temperature. This shows the observed intensity (Y_{obs} —red circles), which is the experimental data, the calculated intensity (Y_{calc} —black line), the difference in observed and calculated intensities ($Y_{\text{obs}} - Y_{\text{calc}}$ —blue line), and peak positions of the phase (green ticks). The calculated parameters of the elementary cell and the

coordinates of the atoms are shown in Table 3. The data at room temperature can be successfully fitted using the orthorhombic $Pbnm$ space group with good reliability factors. Based on the calculation, the symmetry is described as orthorhombic with the following refinement parameters $R_B = 5.89\%$, $R_f = 6.29\%$, and $\chi^2 = 0.347$. It should be noted that the results obtained in this article are consistent with the literature shown elsewhere [30,31].

Table 3. Structural parameters of $SrPbO_3$ at RT and 14 K.

SrPbO ₃ 298 K $Pbnm$					
$a = 5.858$ (1) Å $b = 5.955$ (5) Å $c = 8.326$ (1) Å $V = 290.4$ (8) Å ³					
Ion	X	Y	Z	B (Temp.)	SOF
Sr ⁺²	0.0054 (0)	0.4605 (3)	0.25	0.40 (9)	0.49 (5)
Pb ⁺²	0.0	0.0	0.0	0.11 (6)	0.49 (8)
O ⁻² _I	0.1435 (2)	0.0736 (9)	0.25	0.70 (9)	0.48 (4)
O ⁻² _{II}	0.2136 (4)	0.3055 (2)	−0.0311 (2)	0.89 (6)	0.98 (8)
$R_B = 5.89\%$ $R_f = 6.29\%$ $\chi^2 = 0.347$					
SrPbO ₃ 14 K $Pbnm$					
$a = 5.836$ (2) Å $b = 5.952$ (3) Å $c = 8.294$ (5) Å $V = 288.1$ (4) Å ³					
Ion	X	Y	Z	B (temp.)	SOF
Sr ⁺²	0.0057 (9)	0.4651 (7)	0.25	0.34 (8)	0.50 (5)
Pb ⁺⁴	0.0	0.0	0.0	0.01 (5)	0.47 (9)
O ⁻² _I	0.1582 (9)	0.0515 (0)	0.25	0.61 (5)	0.50
O ⁻² _{II}	0.2253 (0)	0.2833 (0)	−0.0411 (0)	0.69 (9)	0.84 (2)
$R_B = 9.69\%$ $R_f = 13.3\%$ $\chi^2 = 0.347$					

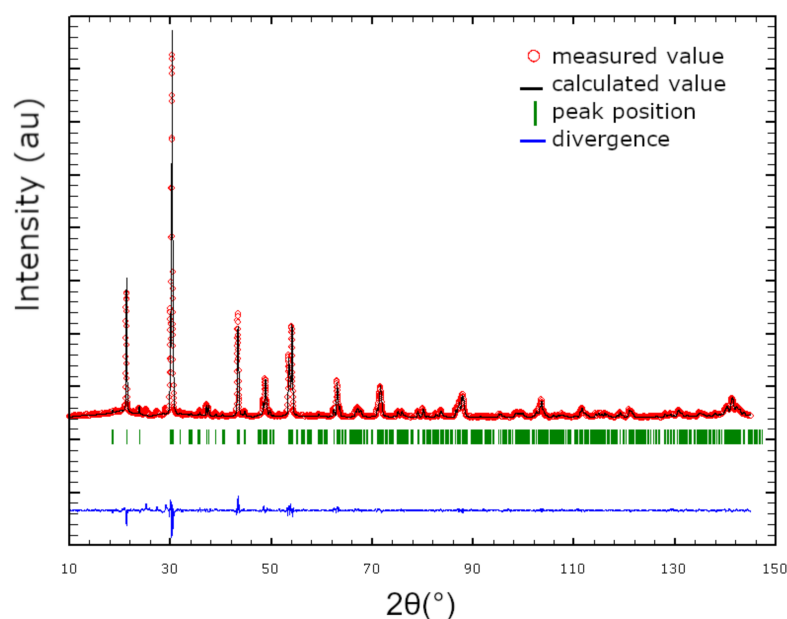


Figure 6. Rietveld analysis results of X-ray powder diffraction pattern for $SrPbO_3$ collected at RT.

3.2. $SrPbO_3$ Ceramic Structure at High and Low Temperatures

Undoped $SrPbO_3$ ceramic was exposed to high (from RT up to 1148 K) and low (from RT up to 14 K) temperatures. The temperature evolution of the selected diffraction lines is shown in Figure 3; it indicates the effect of temperature on the lattice parameters. The sample behavior is remarkable while processing at high temperatures. This behavior is opposite to the behavior of the previously examined oxide perovskite samples containing the PbO_6 octahedral, i.e., $BaPbO_3$ [20]. The temperature relationship of the $SrPbO_3$ pseudocubic cell parameters is shown in Figure 7. It is clear that the cell parameters (a_c, b_c, c_c ,

and β) change smoothly. In other words, they increase systematically with an increase in temperature up to 1093 K. The average error for cell parameters determination was ± 0.0027 Å for a , b , and c ; for β , it was $\pm 0.05^\circ$; and for V , it was equal to ± 0.07 Å³. Widely conducted temperature crystalline structure studies have shown that no structural phase transitions occurred between 298 K and 1093 K in the SrPbO₃ sample. Instead of that, the continuous increase in cell parameters is accompanied by an increase in temperature (Figure 7). This is interesting since Keester et al. [37] reported observing an SPT, a tetragonal phase, that started at about 450 °C. For that reason, special attention was paid in this paper to the 700–770 K temperature range. An analysis of the line splitting showed the presence of three lines of $\{200\}_c$ and $\{220\}_c$ and two lines of $\{222\}_c$ at 723 K (Figure 3). This proves the monoclinic distortion of the perovskite cell. Therefore, this phase cannot be considered as a tetragonal phase since no evidence of the phase was observed. Furthermore, the continuation of high-temperature examinations (up to 1048 K) contradicts literature reports. The proof for this was the constant presence of three $hh0$ diffraction lines and two hhh lines. The linear change of the cell parameters (green squares, blue triangles, and red circles stand for a_c , b_c , c_c , respectively) with increasing temperature was observed, with a clear demonstration that $a_c \approx b_c$ and their values were close to the c_c values. The monoclinic angle (marked with stars). $-\beta-$ tends to a value close to 90° . Therefore, based on the observed behavior, a structural phase transition above the measured temperature of 1093 K can be expected. However, due to further heating, on the sample surface, Sr₂PbO₄ together with PbO was formed. Increasing the temperature inside the HT camera caused the progressive degradation of the sample, which was especially observed at 1148 K. Nevertheless, our study supported data provided by Hester [32], who observed a $Pnma$ structure from 298 to 1033 K.

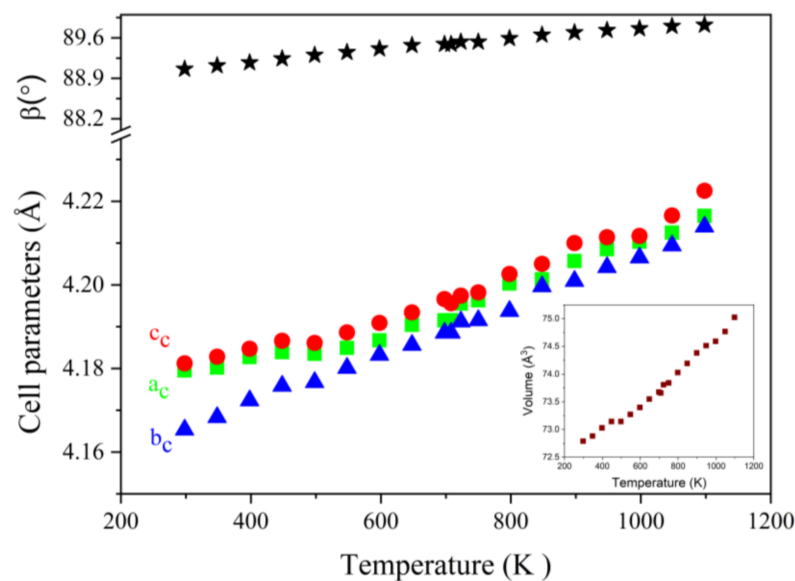


Figure 7. Pseudocubic cell parameters in the function of temperature for SrPbO₃. The inset shows the temperature evolution of the cell volume.

As indicated previously, the crystal structure tests were also performed at low temperatures. The reason for that was that the structural transition to lower symmetry phases was expected to occur. The powder diffraction pattern as low as 14 K, together with Rietveld refinement data from X-ray powder diffraction, are shown in Figure 8 and Table 4, respectively. The analysis indicated that SrPbO₃ has orthorhombic symmetry up to 14 K. It was also concluded that the crystalline structure of SrPbO₃ at 14 K did not show significant differences with respect to the crystalline structure data obtained at RT. The structure can also be described as an orthorhombic $Pbnm$ space group, and cell parameters are $a = 5.836$ (2) Å, $b = 5.952$ (3) Å, $c = 8.294$ (5) Å, $V = 288.1$ (4) Å³. As expected, a volume contraction

was observed, and the temperature factor values decreased. Furthermore, small shifts of the Sr^{2+} cations from their ideal positions in the xy plane were observed, while for O^{2-} additional shifts in the $[001]_c$ direction were observed.

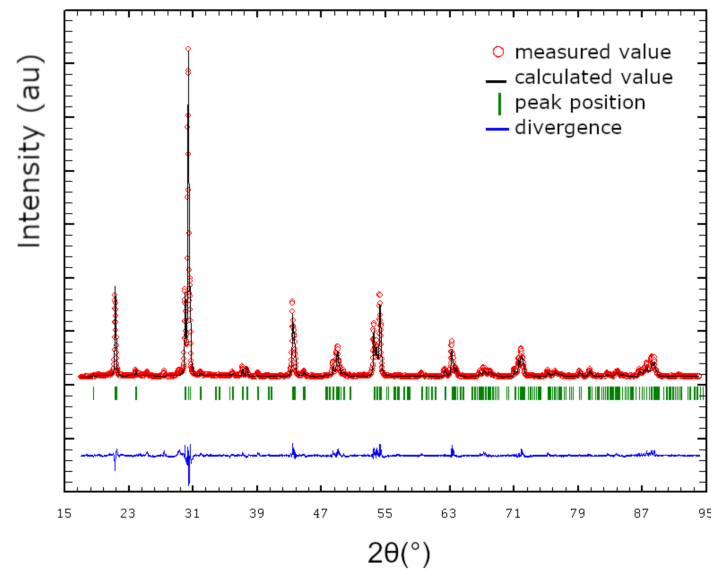


Figure 8. Rietveld analysis results of X-ray powder diffraction pattern for SrPbO_3 collected at 14 K.

Table 4. Selected interatomic distances and angles and estimated tilting angles of PbO_6 for BaPbO_3 , $(\text{Ba}_{0.5}\text{Sr}_{0.5})\text{PbO}_3$, and SrPbO_3 compounds.

Interatomic Distances (Å)/ Interatomic Angles (°)	BaPbO_3	$(\text{Ba}_{0.5}\text{Sr}_{0.5})\text{PbO}_3$	SrPbO_3
Pb-O _I	2.151 (8)	2.297 (2)	2.287 (2)
Pb-O _{II}	2.162 (5)	2.203 (8)	2.223 (2)
Pb-O _{III}	2.165 (4)	2.105 (4)	2.055 (1)
Ba/Sr-O _I	2.140 (5)		
	2.143 (4)		
Ba/Sr-O _I	3.013 (4)	2.253 (1)	2.453 (1)
	2.645 (6)	2.323 (5)	2.160 (5)
	3.081 (1)		
Ba/Sr-O _{II}		3.026 (3)	
	2.799 (9)	2.905 (7)	
	3.260 (8)	2.649 (0)	
		3.020 (2)	2.799 (9)
		2.958 (3)	2.964 (9)
		2.589 (5)	
Ba/Sr-O _{III}	2.864 (6)		
	3.146 (8)		
O _I -Pb-O _{II}	87.1 (7)	84.9 (9)	85.5 (6)
		85.0 (0)	94.4 (3)
O _{II} -Pb-O _{II}		89.2 (3)	90.7 (4)
O _I -Pb-O _{III}	88.1 (2)		
O _{II} -Pb-O _{III}	90.4 (0)		
Tilting angles (°)	BaPbO_3 $a^-b^0c^-$	$(\text{Ba}_{0.5}\text{Sr}_{0.5})\text{PbO}_3$ $a^-a^-c^+$	SrPbO_3 $a^-b^+a^-$
φ_1	10.74	7.88	11.89
φ_2	-	7.88	10.91
φ_3	11.02	10.49	11.89

3.3. Doped Samples

3.3.1. $(\text{Ba}_{0.2}\text{Sr}_{0.8})\text{PbO}_3$ Ceramic Structure Both at RT and HT

Now, it is interesting to evaluate how the substitution of Sr by Ba ions influences the crystal structure. The selected samples contain both $(\text{Ba}_{0.2}\text{Sr}_{0.8})\text{PbO}_3$ and $(\text{Ba}_{0.3}\text{Sr}_{0.7})\text{PbO}_3$ ceramics. As a result of doping with Ba^{2+} to SrPbO_3 , $(\text{Ba}_{0.2}\text{Sr}_{0.8})\text{PbO}_3$ samples were produced. The crystalline structure of the $(\text{Ba}_{0.2}\text{Sr}_{0.8})\text{PbO}_3$ compound was studied in a similar manner, using an undoped sample for the same set of diffraction lines. Therefore, Figure 9 shows the thermal evolution of certain $\{200\}_c$ and $\{222\}_c$ lines at selected temperatures, i.e., at 298 and 1093 K. The analysis of the data showed that the structure has a monoclinic distortion, which is similar to that observed for undoped SrPbO_3 . That conclusion is supported by the presence of three lines of the $\{200\}_c$ type, which exist together with two lines of the $\{222\}_c$ type.

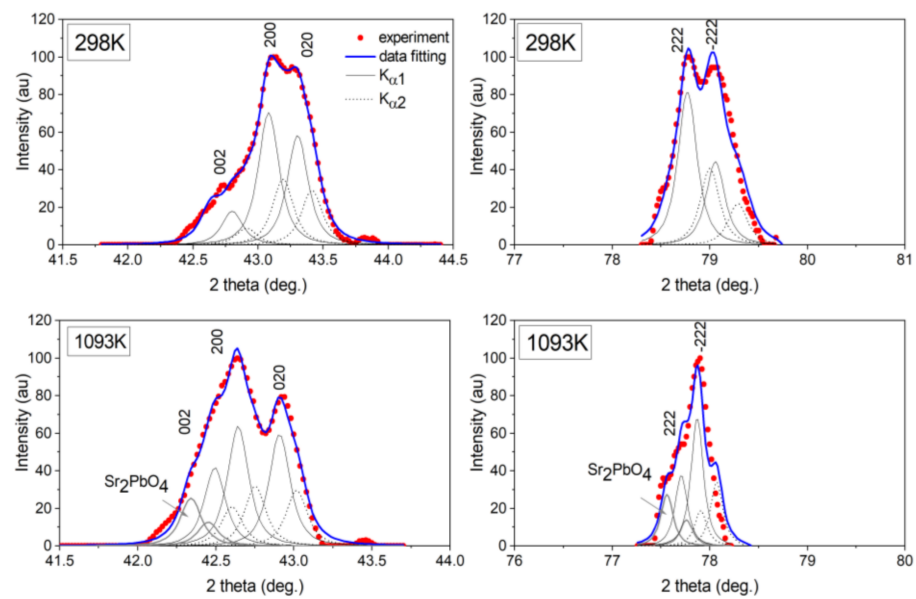


Figure 9. Splitting of the main reflections $\{200\}_c$ and $\{222\}_c$ for $(\text{Ba}_{0.2}\text{Sr}_{0.8})\text{PbO}_3$ at RT and 1093 K.

At 298 K, the splitting analysis of the major diffraction lines indicates a monoclinic distortion of the cell. The reflections resulting from the octahedral tilting in the same direction (+) and in the opposite direction (−) were observed with the indicators for pure SrPbO_3 . For that reason, the tilting of the PbO_6 octahedra can be summarized using Glazer's notation as $a^-b^+c^-$. Based on that, and following Woodward's classification, the pseudocubic cell distortion of $(\text{Ba}_{0.2}\text{Sr}_{0.8})\text{PbO}_3$ can be described as monoclinic with the $P2_1/m$ space group. An analysis showed that in the entire temperature range from 298 K to 1073 K, the $(\text{Ba}_{0.2}\text{Sr}_{0.8})\text{PbO}_3$ sample exhibited monoclinic distortion. Above 1073 K, a structural transition to the tetragonal or orthorhombic phase was expected due to the observable behavior of the cell parameters. However, the further temperature treatment of the sample resulted in the sample decomposition. At 1093 K, some Sr_2PbO_4 was produced on the surface of $(\text{Ba}_{0.2}\text{Sr}_{0.8})\text{PbO}_3$. It was proved by the XRD study that additional diffraction lines were observed at lower 2θ angles, supported by strontium orthoplumbate. This means that 1053 K would be the maximum temperature for its practical application without decomposing the Ba^{2+} -doped sample. Figure 10 shows the temperature evolution of the pseudocubic cell parameters (green squares, blue triangles, and red circles stand for a_c , b_c , c_c , respectively while stars for β) together with the change of the pseudocubic cell volume (brown squares). The monoclinic cells increase in size with an increase in temperature. The average error for the determination of cell parameters was $\pm 0.0039 \text{ \AA}$ for a , b , and c ; for β , it was $\pm 0.11^\circ$; and for V , it was equal to $\pm 0.14 \text{ \AA}^3$. The crystal structure behavior when thermally treated is similar to the behavior observed for

the undoped SrPbO₃ perovskite. SPTs for ceramics (Ba_{0.2}Sr_{0.8})PbO₃ were not observed in the examined temperature range.

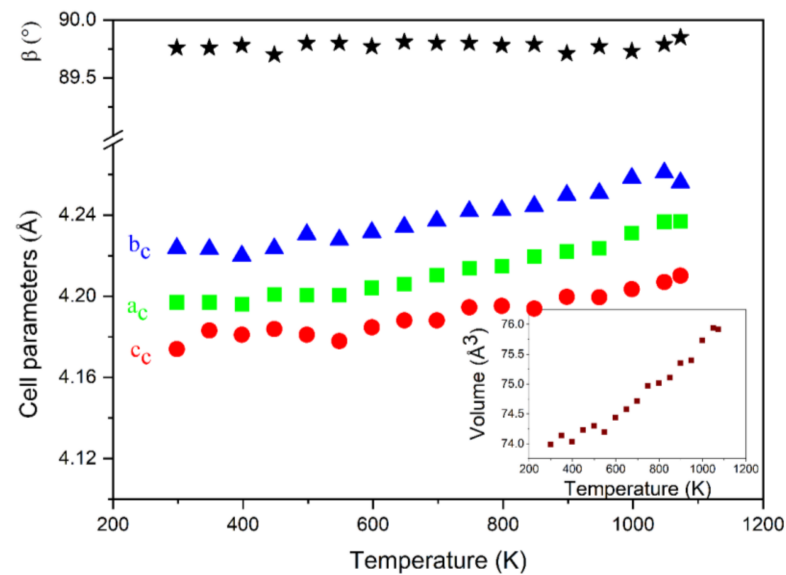


Figure 10. Pseudocubic cell parameters in the function of temperature for (Ba_{0.2}Sr_{0.8})PbO₃.

These results are in opposition to those previously published. This is because [45] suggested that SrPbO₃ does not accept the large Ba ions in the Sr sites and proposed that the limit of substitution is the (Ba_{0.2}Sr_{0.8})PbO₃ sample. In this paper, we proved that the (Ba_{0.2}Sr_{0.8})PbO₃ perovskite is a mono-phase well-crystalized sample that shows monoclinic $P2_1/m$ distortion both at RT and in HT, ranging from 298 K to 1093 K.

3.3.2. (Ba_{0.3}Sr_{0.7})PbO₃ Ceramic Structure Both at RT and HT

The other examined sample doped with Ba²⁺ was (Ba_{0.3}Sr_{0.7})PbO₃. The crystalline structure of the (Ba_{0.3}Sr_{0.7})PbO₃ ceramic was determined at a wide range of temperatures, from 298 K to 1148 K. In Figure 11, the temperature evolution of significant diffraction lines such as $\{200\}_c$ and $\{222\}_c$ at selected temperatures are shown. The analysis of the observed lines at 298 K exhibited the presence of three lines of the $\{200\}_c$ and $\{220\}_c$ type and two lines of the $\{222\}_c$ type. That is to say, monoclinic distortion is observed for the crystal cell where the pseudocubic parameters are $a_c \neq b_c \neq c_c$ and $\beta \neq 90^\circ$. During the high-temperature evaluation of crystal structure behavior, the superstructure lines were observed. Their presence allowed for assigning the PbO₆ tilting type to the corresponding crystal space group. The superstructure lines that were observed in the XRD pattern are caused by octahedral tilting. Tilts of the neighbouring octahedral were detected both in the same direction (+) and in the opposite direction (−), which is similar to that observed for (Ba_{0.3}Sr_{0.7})PbO₃. The presence of odd-odd-odd lines with $k \neq l, h \neq l$ Miller indices such as (−153) and (−531), or (113) clearly indicates PbO₆ octahedra tilting of the a^- and c^- type. The presence of (301), and (−323) superstructure lines with an odd-even-odd parity of reflections with $h \neq l$ indicates that b^+ -type tilting was observed. Furthermore, the presence of superstructure lines such as (124) and (212), (003) indicates that the displacement of Ba²⁺ and Sr²⁺ cations from their ideal positions is taking place. Therefore, both the cation displacement and octahedral tilt affect the distortions of the ideal perovskite cell.

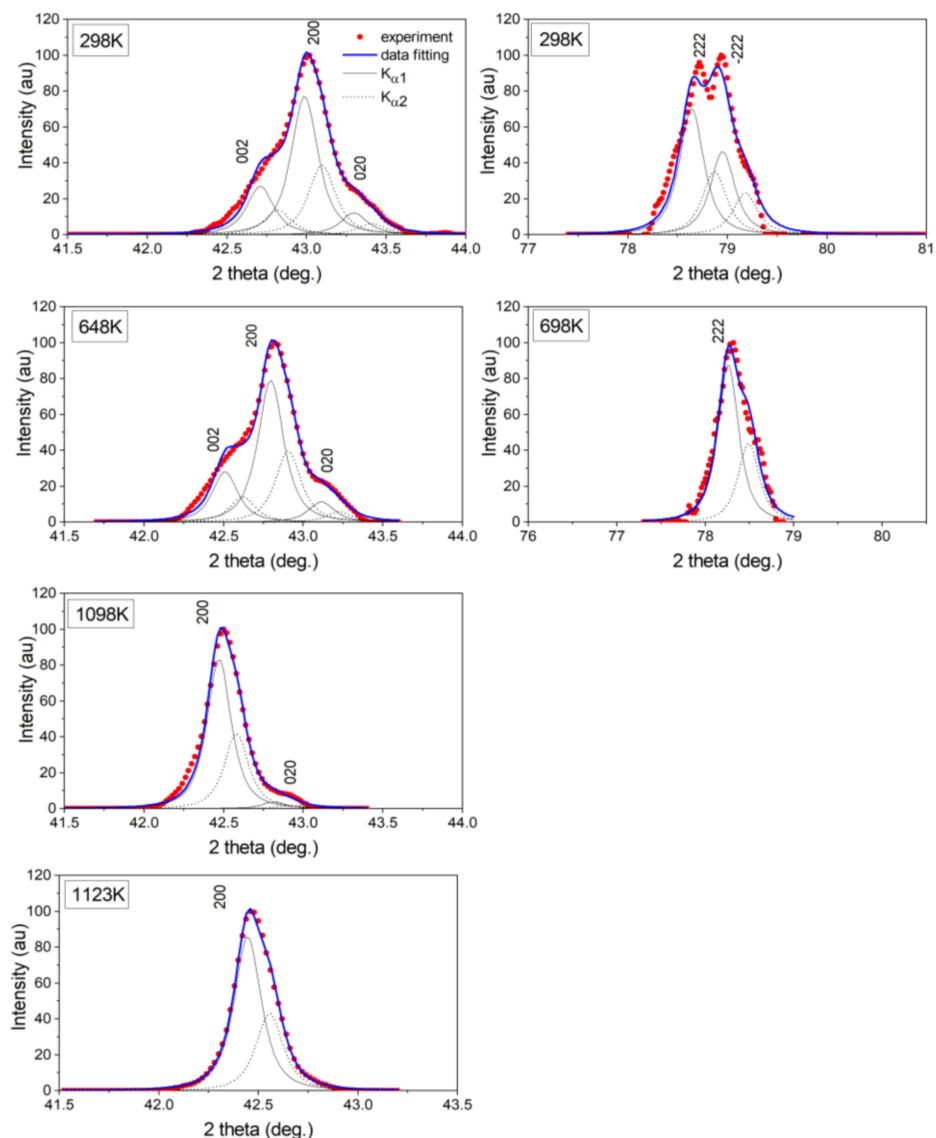


Figure 11. Splitting of the main reflections $\{220\}_c$ and $\{200\}_c$ in different phases for $(\text{Ba}_{0.3}\text{Sr}_{0.7})\text{PbO}_3$.

For this reason, the pseudocubic cell of $(\text{Ba}_{0.3}\text{Sr}_{0.7})\text{PbO}_3$ can be described by $a^-b^+c^-$ notation by assigning the $P2_1/m$ crystal group for pseudocubic cell parameters of $a_c \neq b_c \neq c_c$ and $\beta \neq 90^\circ$.

Further sample heating caused changes in the observed line positions and their number, as it is shown in Figure 11, indicating that structural phase transitions occurred. An analysis carried out at a temperature of 648 K showed the presence of two $\{200\}_c$ lines and one $\{222\}_c$ lines. During sample heating, one of two $\{222\}_c$ lines previously observed at RT has disappeared. Therefore, at 648 K, the first SPT occurred. This means that the monoclinic distortion observed in the crystal cell has transformed into an orthorhombic distortion. The temperature dependence of the pseudocubic cell parameters as a function of temperature is shown in Figure 12. The monotonic increase in the cell parameters is observed when the sample and SPT temperatures are indicated. Moreover, at 648 K, some superstructure lines were observed in the XRD pattern. The superstructure lines (120) and (-201) indicated the displacement of Ba^{2+} and Sr^{2+} cations from their ideal positions—(133) and (-113) —with octahedra tilting of the c^- type, while (-251) , (251) indicated the a^+ type. Using Glazer's notation, $a^+b^0c^-$ is obtained for $(\text{Ba}_{0.3}\text{Sr}_{0.7})\text{PbO}_3$, which indicates the $Pm\bar{m}n$ space group, with the pseudocubic cell parameters described as $b_c < a_c \neq c_c$. The second SPT (orthorhombic–tetragonal transition) was observed at about 1098 K, as shown

in Figures 11 and 12. It is interesting that the tetragonal phase exists in a very narrow temperature range (1098–1123 K), as shown in Figure 12. Moreover, when this SPT is taking place, both cell volume and the cell dimensions suddenly change. This behavior is different from that for $(\text{Ba}_{0.2}\text{Sr}_{0.8})\text{PbO}_3$ and SrPbO_3 . Right behind the tetragonal transformation, the cubic phase was observed at 1123 K. The average error for cell parameters determination was $\pm 0.0032 \text{ \AA}$ for a , b , and c , while for β it was $\pm 0.09^\circ$ and for V it was $\pm 0.11 \text{ \AA}^3$.

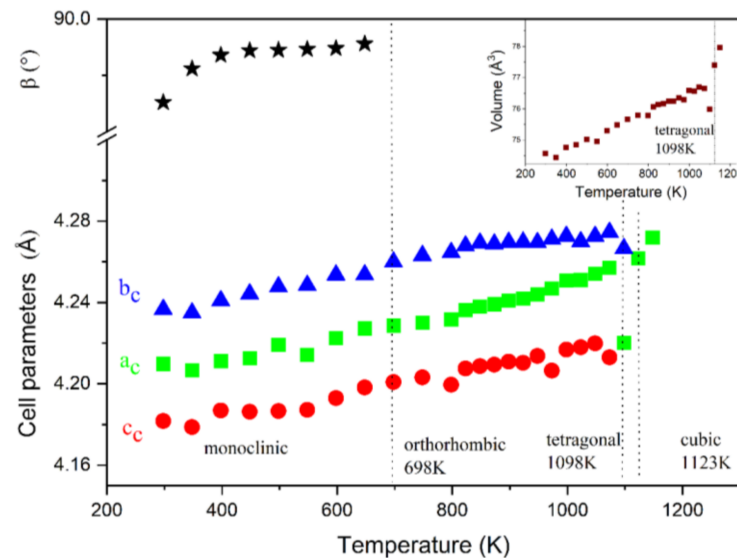


Figure 12. Pseudocubic cell parameters in the function of temperature for $(\text{Ba}_{0.3}\text{Sr}_{0.7})\text{PbO}_3$.

3.4. Discussion on the Crystal Structure of the Oxide Strontium-Barium Perovskites Family

The results on the oxide strontium-barium perovskites family shown in this paper and those previously published [20,42] revealed that it is an interesting group in terms of the meaning of the crystal structure. Moreover, this discussion is applicable to the high-temperature thermoelectric oxide materials of the $(\text{Ba}_{1-x}\text{Sr}_x)\text{PbO}_3$ system, which is capable of converting high-temperature excess heat to electricity and proved to have high thermoelectric figures of merit [7,9].

Detailed X-ray diffraction tests were carried out for the first time for the system on the indicated complexity of the structure. As a result of the examinations, it is concluded that $(\text{Ba}_{0.3}\text{Sr}_{0.7})\text{PbO}_3$ perovskite represents the limit where the substitution of strontium by barium ions in the SrPbO_3 ceramic demonstrates any structural phase transition. This is because for SrPbO_3 and $(\text{Ba}_{0.2}\text{Sr}_{0.8})\text{PbO}_3$ ceramics, no temperature-induced structural phase transition was observed. It means that adding 20% Ba^{2+} to SrPbO_3 did not affect the crystal structure. However, adding 30% Ba^{2+} made a large change, and three SPTs were observed. It is clear that this substitution significantly influenced the crystal structure and evidently the SPTs. In our previous work, a thermal analysis of the structure evolution of BaPbO_3 substituted by Sr ions was carried out, while in the present work strontium-reached samples were examined. Based on the results of this paper and the previous reports, a comparison of two counterparts of the $(\text{Ba}_{1-x}\text{Sr}_x)\text{PbO}_3$ system together with the sample with composition can be conducted. The difference between the crystalline structure of BaPbO_3 and SrPbO_3 is easy to follow. Both structures are monoclinic distortions of the ideal cubic perovskite. BaPbO_3 exhibits slight monoclinic distortion and symmetry, while SrPbO_3 shows monoclinic distortion and orthorhombic symmetry. These distortions are mainly related to the tilting of the oxygen octahedral atom and, to a lesser extent, the A cations from their ideal positions. According to Glazer's classification for BaPbO_3 , these are octahedra tilts of the $a^-b^0c^-$ type, while for SrPbO_3 $a^-b^+a^-$ this tilting is strongly associated with the difference in ion size difference. The ionic radius of Sr^{2+} is smaller than that of Ba^{2+} ; they are $R_{XII\text{Sr}2+} = 1.44 \text{ \AA}$ and $R_{XII\text{Ba}2+} = 1.61 \text{ \AA}$, respectively. If cation A is smaller than the oxygen ions, the PbO_6 octahedra may tilt towards one another to reduce

the size of the cavity, which is occupied by cation *A*. This leads to an increase in tilt angle. PbO_6 tilt angles were estimated for both materials and were equal to 10.74 and 11.02° for BaPbO_3 , while they were 11.89, 10.91, and 11.89° for SrPbO_3 (Table 4). Furthermore, in both structures, Pb^{4+} ions occupy specific positions, remaining centrosymmetric. However, for the BaPbO_3 compound, a small displacement of Ba^{2+} from its ideal position in the *xz* plane of $\Delta x = 0.0024$ and $\Delta z = -0.0168$ is observed. In contrast, Sr^{2+} ions in the SrPbO_3 ceramic are moved towards the *xy* plane by about $\Delta x = 0.0054$ and $\Delta y = -0.0405$. It is clear that the displacement of Sr^{2+} ions is much greater than that of Ba^{2+} ions. It results in changes in PbO_6 octahedra, and for BaPbO_3 ceramics, the PbO_6 octahedra are only slightly changed in shape. However, in SrPbO_3 , the material distortion of the structure is much larger due to the larger octahedral tilting angles, as can be seen in Figure 5. As a result, the *Pb*-*O* distance for SrPbO_3 is 2.287 (2) Å, while for BaPbO_3 , it is 2.151 (8) Å. The cell parameters of SrPbO_3 are smaller compared to BaPbO_3 . The angles of O_I -*Pb*- O_II and O_II -*Pb*- O_II for SrPbO_3 are 85.5 (6)°, 94.4 (3)°, and 90.7 (4)°, respectively, and for BaPbO_3 O_I -*Pb*- O_II , O_II -*Pb*- O_III and O_I -*Pb*- O_III they are 87.1 (7)°, 90.4 (0)°, and 88.1 (2)°. It is clear that for SrPbO_3 the deviation from the 90° angle is much higher (Table 4). When examining the sample with *x* = 0.5, where equal amounts of Ba^{2+} and Sr^{2+} ions were incorporated into the crystal structure, the values of angles of octahedra tilting were, as expected, an average value for their counterparts. Furthermore, when Sr^{2+} was added to pure BaPbO_3 , an additional tilt was observed [42], as can be seen in Table 4.

Furthermore, the comparison shows that barium substitution with strontium in the BaPbO_3 ceramic results in a decrease in the structure tolerance factor. As the data from the literature showed, for BaPbO_3 τ was equal to 0.985 [20], while for $(\text{Ba}_{0.5}\text{Sr}_{0.5})\text{PbO}_3$ it was 0.957 [42] and for SrPbO_3 it was 0.928. This change may be an indication of possible crystal structure deviations, and greater distortion may be expected. This was supported experimentally (Table 4). For BaPbO_3 , there are two types of octahedral tilting in the opposite direction (−) that can be described as $a^-b^0c^-$. For $(\text{Ba}_{0.5}\text{Sr}_{0.5})\text{PbO}_3$, there appears to be additional tilting in the same direction (+) $a^-a^-c^+$, while for the SrPbO_3 sample, there is the $a^-b^+a^-$ tilting type.

The data from the present work and previous papers [20,42] on crystal structure as a function of temperature enabled us to gain a complete understanding of the $(\text{Ba}_{1-x}\text{Sr}_x)\text{PbO}_3$ perovskite system. It should be emphasized that in this work detailed data were shown specifically for $(\text{Ba}_{0.3}\text{Sr}_{0.7})\text{PbO}_3$, $(\text{Ba}_{0.2}\text{Sr}_{0.8})\text{PbO}_3$ and SrPbO_3 samples. The extended study enabled the evaluation of the temperature behavior of the crystal structure. As a result of this wide-ranging study, based on the recent and already published co-authored papers, Figure 13 shows pseudocubic cell parameters as a function of composition for the whole $(\text{Ba}_{1-x}\text{Sr}_x)\text{PbO}_3$ family. Since interesting results were obtained for the concentrations of Sr^{2+} ions (*x* = 0, 0.2, 0.5, 0.8, and 1.0, etc.), additional samples (of 0.1 and 0.9, etc.) were additionally produced. Due to the fact that an enormous amount of data was collected during the extensive research, only some data were shown in the manuscript. Consequently, this has resulted in the preparation of Figures 13 and 14.

It is clear that the addition of Sr^{2+} ions to BaPbO_3 led to a decrease in cell parameters as the amount of Sr increased in the sample. It can be seen that the difference between pseudocubic parameters a_c , b_c , and c_c also slowly decreased with the substitution degree. For the sample $(\text{Ba}_{0.5}\text{Sr}_{0.5})\text{PbO}_3$ with *x* = 0.5, all three pseudocubic parameters are almost equal. This behavior may result from equal amounts of both Ba^{2+} and Sr^{2+} ions. This caused a type of competition between these two ions, which were substituting the same ion place, finally leading to almost the same pseudocubic cell parameter values. For the $(\text{Ba}_{1-x}\text{Sr}_x)\text{PbO}_3$ system, which is found to be practically attractive due to its metallic conduction and semiconduction properties, the mobility of electrons was seriously influenced by the randomness of cations at the A-site [35]. In fact, the resistivity increased with *x* and the metallic behavior disappeared for the $(\text{Ba}_{0.5}\text{Sr}_{0.5})\text{PbO}_3$ sample. This is because the carrier concentration decreased rapidly when *x* > 0.5 and the mobility of electrons in the $(\text{Ba}_{1-x}\text{Sr}_x)\text{PbO}_3$ system showed a minimum at *x* = 0.5. Because the substitution of Ba^{2+}

by Sr^{2+} ions leads to the lattice, it also leads to the change in the local symmetry of the octahedra. The overlap between the Pb 6s and O 2p orbitals is the origin of the metallic conductivity of this system. Since the local symmetry of PbO_6 octahedra is changed, it results in the narrowing of the Pb 6s–O 2p conduction band, and finally, it affects the density of states in the Fermi surface.

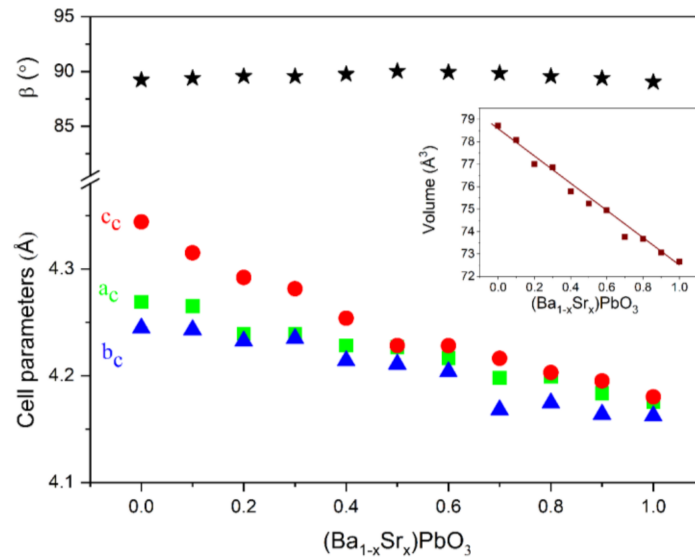


Figure 13. The pseudocubic cell parameters in function of composition for $(\text{Ba}_{1-x}\text{Sr}_x)\text{PbO}_3$ system.

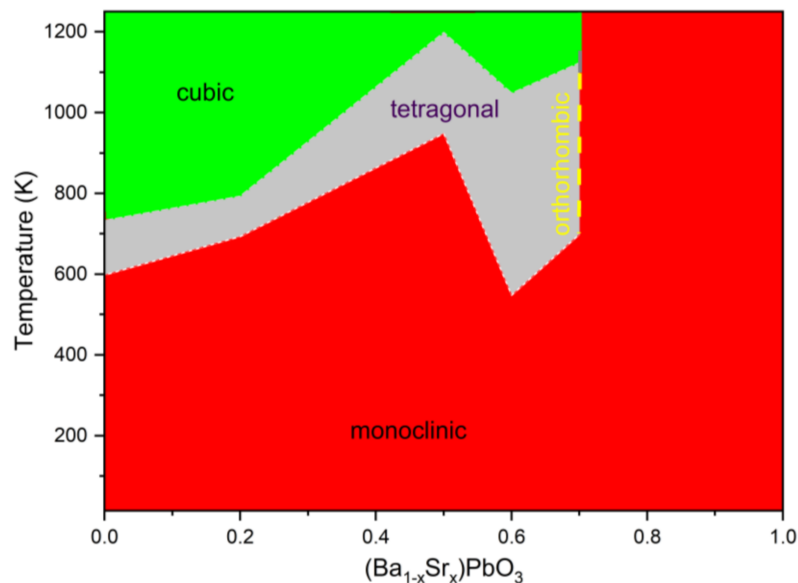


Figure 14. Phase diagram for $(\text{Ba}_{1-x}\text{Sr}_x)\text{PbO}_3$ system.

Analogously, the inset in Figure 13 shows, that the volume of the pseudocubic cell changed linearly with the degree of substitution. The analysis of the XRD pattern at RT showed that the distortion for SrPbO_3 was significantly bigger than that observed for BaPbO_3 , with middle values for intermediate compositions.

What is fundamental is that the XRD, together with SEM-EDS data, proved that it was possible to obtain good-quality monophasic samples, which is in opposition to some previous reports [45]. Furthermore, it is also the first time that such a wide-temperature study has been carried out. The obtained results from X-ray powder diffraction measurements allowed us to prepare the phase diagram for $(\text{Ba}_{1-x}\text{Sr}_x)\text{PbO}_3$ samples, which is

shown in Figure 14. In Figure 14, three regions, namely monoclinic (red area), tetragonal distortion (grey area), and cubic (green area), are marked. The phase diagram is built based on a careful investigation, covering temperatures in the 14–1148 K range and substitution levels from 0 to 1.0 in the $(\text{Ba}_{1-x}\text{Sr}_x)\text{PbO}_3$ system. Taken together, the data obtained in the presented work and the data obtained in the previous papers enabled us to build this diagram. Lower-temperature studies proved that the system exists as a monoclinic distortion of the perovskite cell in the whole substitution range. Moreover, at room temperature, all studied ceramics showed monoclinic distortion. It is clear that the monoclinic distortion is dominant when looking closely at the diagram. When the temperature increases, monoclinic-tetragonal phase transitions occur for substitutions of 0 to 0.7. For example, for parent ceramic BaPbO_3 , monoclinic distortion existed up to 598 K; for substituted $(\text{Ba}_{0.8}\text{Sr}_{0.2})\text{PbO}_3$, it existed up to 693 K; for $(\text{Ba}_{0.5}\text{Sr}_{0.5})\text{PbO}_3$ it was up to 948 K; and for $(\text{Ba}_{0.4}\text{Sr}_{0.6})\text{PbO}_3$ and $(\text{Ba}_{0.3}\text{Sr}_{0.7})\text{PbO}_3$ ceramics it was, respectively, 548 K and 1098 K. On this basis, it can be concluded that the temperature of the structural phase transition increases while increasing the amount of Sr^{2+} in the sample, except for in the $(\text{Ba}_{0.4}\text{Sr}_{0.6})\text{PbO}_3$ sample, which is not clear. The detected tetragonal phase (a grey area) is rather narrow for the system. Furthermore, similar behavior is also observed when the experimental temperature is increased, where the tetragonal-cubic transition occurs. For barium-rich samples such as BaPbO_3 or $(\text{Ba}_{0.8}\text{Sr}_{0.2})\text{PbO}_3$, cubic phases exist as low as 733 K and 793 K. Cubic structure is observed for $(\text{Ba}_{1-x}\text{Sr}_x)\text{PbO}_3$ materials where $x = 0-0.7$. For ceramics with $x > 0.7$, no structural temperature-induced phase transitions are observed during pendant heating.

The detailed explanation of the relationship between structural distortions of the $(\text{Ba}_{1-x}\text{Sr}_x)\text{PbO}_3$ materials, together with transitions and physical properties, is included below. The BaPbO_3 dense ceramic was proposed as an electrode material for ferroelectric thin films [35,46,47]. For the temperature-dependence of thermal conductivity, a decrease in the value was observed at ca. 450 °C (723 K) [46]. This behavior correlates well with our data, which showed that at 733 K (460 °C) a tetragonal-cubic transition occurs. SrPbO_3 is known as a n-type narrow-bandgap semiconductor, exhibiting a semiconducting behavior that is ascribed to the electropositive character of Sr and the constancy of the valence band energy of O^{2-} :2p parentage. SrPbO_3 offers the possibility of constructing solar devices [47]. It reported that the weak hybridization of the PbO bond, due to the tilting of the octahedra, beneficially reduces the energy of the antibonding conduction band, resulting in a small optical gap E_g (1.76 eV). For this reason, the following features allow the material to be used in solar energy conversion: sufficient negative potential V_{fb} , an optical gap value close to the optimal value required for terrestrial applications, and good chemical stability, which is proved in our experiments. During the heating, the SrPbO_3 ceramic structure with monoclinic distortion is stable without decomposing (Figure 14). However, the maximum working temperature cannot exceed 1093 K, as demonstrated.

In Figure 15, simultaneous thermal analysis data are shown for selected perovskites of the $(\text{Ba}_{1-x}\text{Sr}_x)\text{PbO}_3$ system. A 5 mg sample was analyzed in each case within the conditions described in the experimental section. Figure 15a,b shows the experimental data for the two non-doped perovskites, i.e., BaPbO_3 and SrPbO_3 , respectively. The mass changes of the samples were observed in the given regions where structural phase transitions appeared. It is clear to see small slopes in masses, shown in the circles, supporting SPT for BaPbO_3 . The existence of the phases, namely by the structural distortion of ideal perovskites, is shown by diverse fields with different patterns filled. However, it should be noted that there were no changes in temperature (DSC) observed while SPT occurred, nor when the initial mass of the sample was changed from 5 to 20 or 200 mg. Furthermore, when the structural phase transitions were not detected by XRD study, they were also not observed in STA examinations, as shown, for example, for the SrPbO_3 material. The thermal analyzer used in this research was a valuable tool with great accuracy and sensitivity, enabling supporting observations from powder diffraction. As a consequence, this supplementary testing supported the XRD data and enabled the preparation of the phase diagram.

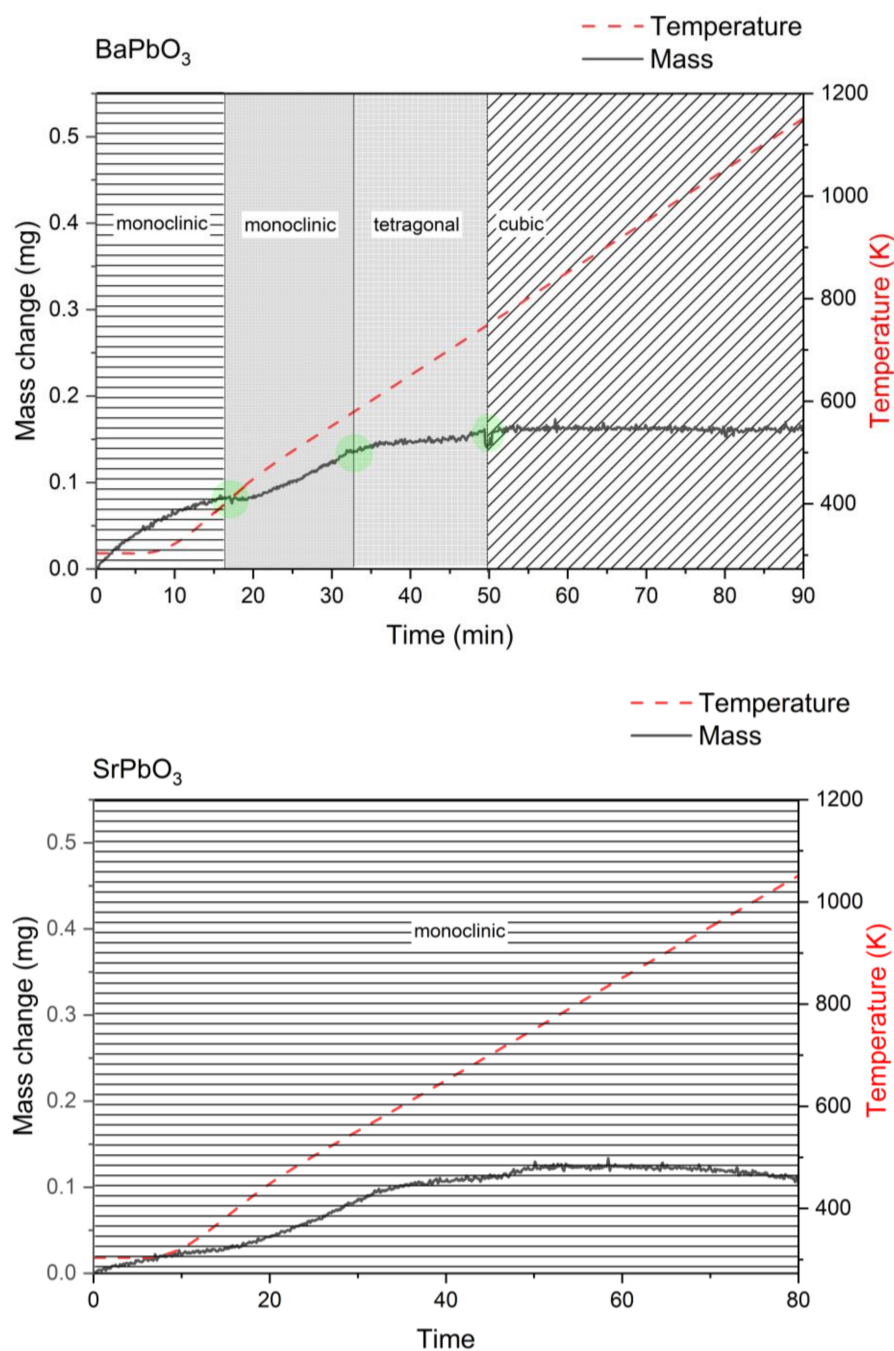


Figure 15. STA analysis for selected examples of BaPbO₃ and SrPbO₃ perovskites.

3.5. Potential Application in Different Processes

The literature study showed that no prior experiments determined that feature perovskites (Ba,SrPbO₃) were tested as oxygen carriers (OCs). In this experiment, the selected samples (SrPbO₃, BaPbO₃, and Ba_{0.9}Sr_{0.1}PbO₃) were used as an OC for solid fuel combustion. Preliminary tests have been performed using graphite as an initial fuel. Tests with graphite proved that combustion with fuel is possible at temperatures as low as 800 °C (1073 K); however, reaction occurs very slowly, and fuel conversion rates were low. At 900 °C (1173 K), the fuel conversion of graphite reached almost 100%. However, sample SrPbO₃ melted in this temperature, and XRD analysis showed the decomposition of this material. Therefore, for the next investigation with this material, the sample was tested at a lower temperature 850 °C (1123 K). In Figure 14, SrPbO₃ shows a maintained monoclinic structure in our temperature measurement range, while more barium-rich perovskites un-

derwent phase transition to tetragonal, and finally cubic, structures at higher temperatures. This might indicate that monoclinic perovskites of this series are less temperature-stable. In the next step, the analysis was performed with the Illinois#6 hard coal to check the perovskite performance in the chemical looping combustion (CLC) process with a real fuel. The TGA analysis revealed that the mass changed throughout the time of the combustion at 850 and 900 °C (1173 K) (Figure 16). The graphs also provide additional data from mass spectrometry (QMS) that show the production of H₂O and CO₂ during the process. The emission of those gases corresponds to mass changes observed during TGA experiments, which supports that the combustion process took place. The combustion occurs in several stages, which is clear from Figure 16. Using the TGA data, the amount of oxygen release was calculated for the samples. For SrPbO₃, BaPbO₃, and Ba_{0.9}Sr_{0.1}PbO₃, values were 2.6, 2.8, and 3.6 wt.%, respectively. The materials were also regenerated by using a stream of air. The regeneration showed faster kinetics (green area) compared to the combustion process (grey area).

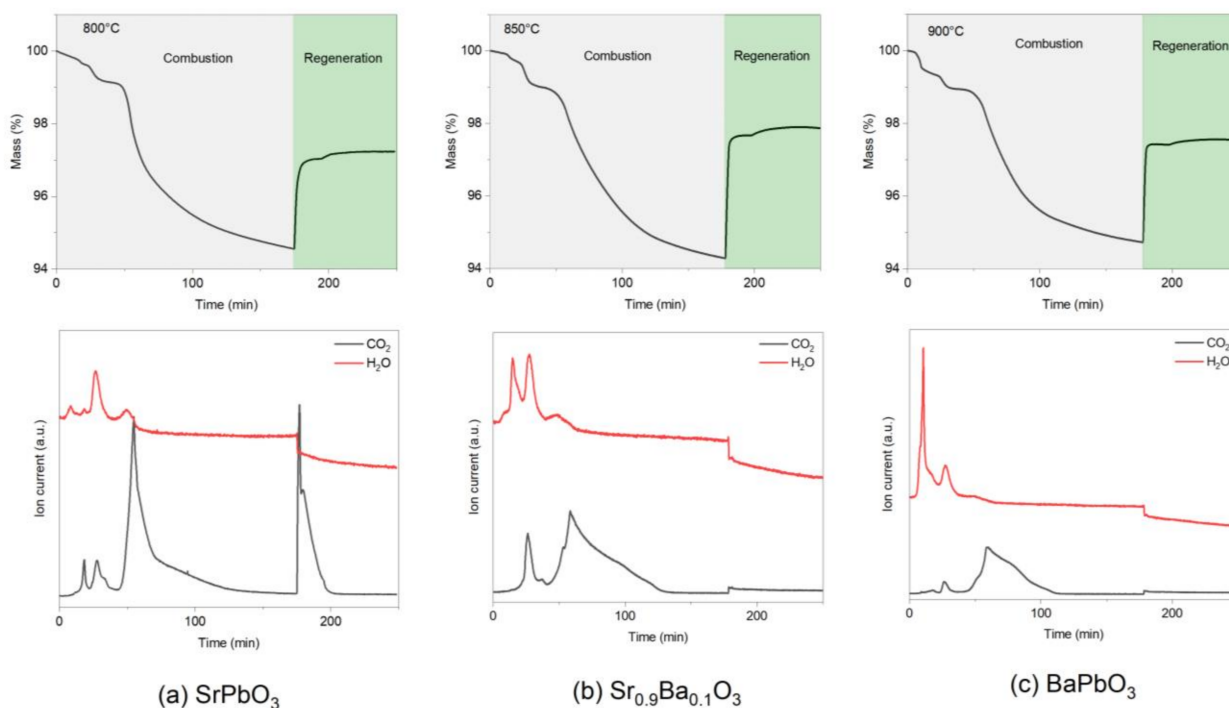


Figure 16. TGA-QMS analysis for selected samples of SrPbO₃, Ba_{0.9}Sr_{0.1}PbO₃ and BaPbO₃ perovskites.

Due to the low melting temperature for the SrPbO₃ sample, the combustion of the fuel was not performed effectively at some temperatures. For example, in Figure 16a, the high peak of CO₂ is presented during regeneration, which means not all coal was combusted completely at 850 °C (1123 K). However, for BaPbO₃, which is more thermally stable, total hard coal combustion was observed even as high 900 °C (1173 K) (Figure 16c). This is distinguished by elevated CO₂ peaks during combustion and the lack of a CO₂ peak in the regeneration stage. When barium was added to SrPbO₃, an improvement in thermal stability and reactivity were observed (Figure 16b). The Ba_{0.9}Sr_{0.1}PbO₃ might be indicated as the promising sample for CLC application. Consequently, the high content of barium increases the temperature resistivity; moreover, a small addition of strontium provides a beneficial reactivity rate. Therefore, the Sr-doped material showed the better performance with the Illinois#6 hard coal.

4. Conclusions

In conclusion, this paper covers a complementary and detailed study of the structural properties of $(\text{Ba}_{1-x}\text{Sr}_x)\text{PbO}_3$. XRD was used for the investigations of ceramics implemented in practice as high-performance oxide ceramics used as high-temperature thermoelectric energy-conversion materials or for preventing the corrosion of long-life batteries. The crystalline structure and the temperature-dependent variation of the series were determined for the first time by obtaining good-quality samples, which were also proved by SEM–EDS examination. The type of distortion and symmetry of the synthesized perovskites were determined in a wide range of temperatures, from 14 K to 1148 K. The types of splitting and the numbers of the main diffraction lines, which are produced by different sequences of the tilts of the oxygen octahedral, were analyzed. For each symmetry, the parameters of the crystalline structure were determined. Several samples from the $(\text{Ba}_{1-x}\text{Sr}_x)\text{PbO}_3$ series were selected, such as $(\text{Ba}_{0.3}\text{Sr}_{0.7})\text{PbO}_3$, $(\text{Ba}_{0.2}\text{Sr}_{0.8})\text{PbO}_3$ and SrPbO_3 . On the basis of that, the crystal structure distortion of SrPbO_3 was monoclinic at RT. XRD measurements carried out for SrPbO_3 over a wide temperature range did not confirm any occurrence of structural phase transitions, as previously suggested in the literature. The limit of substitution was determined for the substitution of ions in site A, for which structural phase transitions are still observed at 30% of Ba and 70% of Sr. Thus, for the $(\text{Ba}_{0.2}\text{Sr}_{0.8})\text{PbO}_3$ perovskite, no structural changes are observed. This sample was stable over a broad temperature range and exhibited monoclinic distortion.

Furthermore, in this work, simultaneous thermogravimetry–differential scanning calorimetry and STA/TG–DSC were applied. The instrument was also coupled to a quadrupole mass spectrometer (QMS). The thermal analysis examinations for obtained perovskites supported both XRD and EDS findings. This comprehensive study was essential and supported the observations of SPTs, as well as the great thermal stability of perovskites, together with ceramics composition.

What is fundamental, is that the XRD, together with SEM–EDS examination data, proved that it was possible to obtain mono-phase samples of good quality, which is in opposition to some reports. Furthermore, it is also the first time that such a wide-temperature study has been carried out. Structural phase transitions were observed for solid solutions of $(\text{Ba}_{1-x}\text{Sr}_x)\text{PbO}_3$ and were described in detail, allowing for the preparation of the phase diagram.

A detailed explanation of the relationship between structural distortions of the materials and the physical properties is included in this paper. Practically, our study proved that the materials are stable even at a temperature as high as ca. 1050 K for strontium-rich samples, such as $(\text{Ba}_{0.2}\text{Sr}_{0.8})\text{PbO}_3$ or SrPbO_3 , as well as more resistant. This temperature was proven to be ca. 1200 K for barium-rich samples such as $(\text{Ba}_{0.4}\text{Sr}_{0.6})\text{PbO}_3$ and $(\text{Ba}_{0.5}\text{Sr}_{0.5})\text{PbO}_3$, without decomposition. Stable performance is possible even for a high degree of substitution due to the shift of cations from their ideal positions and octahedral titling. These ceramics are examples of thermoelectric oxide materials that are capable of converting high-temperature excess heat to electricity. Furthermore, some ceramics, such as optically active semiconductor oxides such as SrPbO_3 or $(\text{Ba}_{0.2}\text{Sr}_{0.8})\text{PbO}_3$, offer the possibility of constructing solar devices; by the conversion of light, electrical energy can be generated.

In this paper, for the first time, the investigation of a new application was presented for the $(\text{Ba}_{1-x}\text{Sr}_x)\text{PbO}_3$ family. The TGA analysis was performed with Illinois#6 hard coal to check perovskites performance in the chemical looping combustion (CLC) process. Finally, $\text{Ba}_{0.9}\text{Sr}_{0.1}\text{PbO}_3$ was indicated to have the most potential for application as an oxygen carrier due to its thermal stability and reactivity.

Author Contributions: E.K.: conception of the work, samples synthesis, XRD and SEM–EDS experiments and analysis, manuscript writing, R.L.: STA acquisition and TGA–QMS data analysis, M.A.: language correction and formatting, drafting the TGA work. All authors have read and agreed to the published version of the manuscript.

Funding: This research received no external funding.

Conflicts of Interest: The authors declare no conflict of interest.

References

1. Lee, S.; Cho, J.S.; Kang, D.W. Perovskite/Polyethylene Oxide Composites: Toward Perovskite Solar Cells without Anti-Solvent Treatment. *Ceram. Int.* **2019**, *45*, 23399–23405. [\[CrossRef\]](#)
2. Geffroy, P.M.; Vivet, A.; Guironnet, L.; Richet, N.; Rossignol, F.; Chartier, T. Perovskite Foams Used in Combination with Dense Ceramic Membranes for Oxygen Transport Membrane Applications. *Ceram. Int.* **2018**, *44*, 19831–19835. [\[CrossRef\]](#)
3. Rosa Silva, E.; Nicolini, J.V.; Yamauchi, L.; Machado, T.M.; Curi, M.; Furtado, J.G.; Secchi, A.R.; Ferraz, H.C. Carbon-Based Electrode Loaded with Y-Doped SrTiO₃ Perovskite as Support for Enzyme Immobilization in Biosensors. *Ceram. Int.* **2020**, *46*, 3592–3599. [\[CrossRef\]](#)
4. Haye, E.; Capon, F.; Barrat, S.; Boulet, P.; Andre, E.; Carteret, C.; Bruyere, S. Properties of Rare-Earth Orthoferrites Perovskite Driven by Steric Hindrance. *J. Alloys Compd.* **2016**, *657*, 631–638. [\[CrossRef\]](#)
5. Huang, L.; Xu, J.; Sun, X.; Li, C.; Xu, R.; Du, Y.; Ni, J.; Cai, H.; Li, J.; Hu, Z.; et al. Low-Temperature Photochemical Activation of Sol-Gel Titanium Dioxide Films for Efficient Planar Heterojunction Perovskite Solar Cells. *J. Alloys Compd.* **2018**, *735*, 224–233. [\[CrossRef\]](#)
6. Zdorovets, M.; Kozlovskiy, A.; Arbut, A.; Tishkevich, D.; Zubar, T.; Trukhanov, A. Phase Transformations and Changes in the Dielectric Properties of Nanostructured Perovskite-like LBZ Composites as a Result of Thermal Annealing. *Ceram. Int.* **2020**, *46*, 14460–14468. [\[CrossRef\]](#)
7. Itoh, M.; Sawada, T.; Kim, I.S.; Inaguma, Y.; Nakamura, T. Electrical Properties of the A(Pb_{1-x}B_x)O_{3-δ} (A = Ba, Sr, B = Sb, Bi) System. *Phys. C Supercond.* **1992**, *204*, 194–202. [\[CrossRef\]](#)
8. Che, W.; Wei, M.; Sang, Z.; Ou, Y.; Liu, Y.; Liu, J. Perovskite LaNiO_{3-δ} Oxide as an Anion-Intercalated Pseudocapacitor Electrode. *J. Alloys Compd.* **2018**, *731*, 381–388. [\[CrossRef\]](#)
9. Drozd, V.A.; Ekino, T.; Gabovich, A.M.; Pękała, M.; Ribeiro, R.A.; Shevchenko, A.D.; Uvarov, V.M. Current Carrier Localization and Coulomb Gap Observed in SrPbO_{3-δ} by Transport Measurements and Tunnel Spectroscopy. *J. Phys. Condens. Matter.* **2005**, *17*, 7407. [\[CrossRef\]](#)
10. Oanh Vu, T.K.; Kim, Y.H.; Ahn, C.W.; Kim, M.H.; Han, I.K.; Kim, E.K. Optimization of Optoelectrical Properties during Synthesizing Methylammonium Lead Iodide Perovskites via a Two-Step Dry Process. *J. Mater. Res. Technol.* **2021**, *14*, 1–9. [\[CrossRef\]](#)
11. Rajeswari, R.; Islavath, N.; Raghavender, M.; Giribabu, L. Recent Progress and Emerging Applications of Rare Earth Doped Phosphor Materials for Dye-Sensitized and Perovskite Solar Cells: A Review. *Chem. Rec.* **2020**, *20*, 65–88. [\[CrossRef\]](#)
12. Zhang, C.; Zeng, K.; Wang, C.; Liu, X.; Wu, G.; Wang, Z.; Wang, D. LaMnO₃ Perovskites via a Facile Nickel Substitution Strategy for Boosting Propane Combustion Performance. *Ceram. Int.* **2020**, *46*, 6652–6662. [\[CrossRef\]](#)
13. Qiu, J.; Yang, S. Material and Interface Engineering for High-Performance Perovskite Solar Cells: A Personal Journey and Perspective. *Chem. Rec.* **2020**, *20*, 209–229. [\[CrossRef\]](#)
14. Zhuang, S.; Han, N.; Chen, R.; Yao, Z.; Zou, Q.; Song, F. Perovskite Oxide Based Composite Hollow Fiber Membrane for CO₂ Transport. *Ceram. Int.* **2020**, *46*, 2538–2544. [\[CrossRef\]](#)
15. Zhang, H.; Guan, D.; Gao, X.; Yu, J.; Chen, G.; Zhou, W.; Shao, Z. Morphology, Crystal Structure and Electronic State One-Step Co-Tuning Strategy towards Developing Superior Perovskite Electrocatalysts for Water Oxidation. *J. Mater. Chem. A* **2019**, *7*, 19228–19233. [\[CrossRef\]](#)
16. Das, N.; Kumar, S.; Kumar, V.; Jain, N.; Singh, S.; Gupta, L.C.; Ganguli, A.K. LnFe_{0.5}Cr_{0.5}O₃ Based Perovskites Showing Multiferroic Properties and Polarization Induced Photoelectrochemical Activity. *J. Solid State Chem.* **2021**, *299*, 122200. [\[CrossRef\]](#)
17. Ksepko, E. Perovskite Sr(Fe_{1-x}Cu_x)O_{3-δ} Materials for Chemical Looping Combustion Applications. *Int. J. Hydrogen Energy* **2018**, *43*, 9622–9634. [\[CrossRef\]](#)
18. Ksepko, E.; Lysowski, R. Effective Direct Chemical Looping Coal Combustion Using Bimetallic Ti-Supported Fe₂O₃-MnO₂ Oxygen Carriers. *Greenh. Gases Sci. Technol.* **2023**. [\[CrossRef\]](#)
19. Ksepko, E.; Lysowski, R. Extremely Stable and Durable Mixed Fe–Mn Oxides Supported on ZrO₂ for Practical Utilization in CLOU and CLC Processes. *Catalysts* **2021**, *11*, 1285. [\[CrossRef\]](#)
20. Ksepko, E.; Ratuszna, A. Crystal Structure and Temperature Dependent Structural Phase Transitions in (Ba_{1-x}Sr_x)PbO₃ (X = 0, 0.2, 0.6) Perovskite Ceramics. *Ceram. Int.* **2018**, *44*, 18294–18302. [\[CrossRef\]](#)
21. Li, C.; Wang, A.; Xie, L.; Deng, X.; Liao, K.; Yang, J.A.; Li, T.; Hao, F. Emerging Alkali Metal Ion (Li⁺, Na⁺, K⁺ and Rb⁺) Doped Perovskite Films for Efficient Solar Cells: Recent Advances and Prospects. *J. Mater. Chem. A* **2019**, *7*, 24150–24163. [\[CrossRef\]](#)
22. Qin, C.; Matsushima, T.; Klotz, D.; Fujihara, T.; Adachi, C.; Qin, C.; Matsushima, T.; Adachi, C.; Klotz, D.; Fujihara, T. The Relation of Phase-Transition Effects and Thermal Stability of Planar Perovskite Solar Cells. *Adv. Sci.* **2019**, *6*, 1801079. [\[CrossRef\]](#) [\[PubMed\]](#)
23. Soliman, N.K. Factors Affecting CO Oxidation Reaction over Nanosized Materials: A Review. *J. Mater. Res. Technol.* **2019**, *8*, 2395–2407. [\[CrossRef\]](#)
24. Yasukawa, M. High-Temperature Thermoelectric Properties of the Solid Solutions BaBi_{1-x}Pb_xO₃ (X = 0–1). *J. Mater. Sci. Lett.* **2001**, *20*, 1493–1495. [\[CrossRef\]](#)

25. Shin, W.; Murayama, N.; Ikeda, K.; Sago, S. Thermoelectric Power Generation Using Li-Doped NiO and (Ba, Sr)PbO₃ Module. *J. Power Sources* **2001**, *103*, 80–85. [[CrossRef](#)]
26. Shin, W.; Murayama, N.; Ikeda, K.; Sago, S.; Terasaki, I. Thermoelectric Device of Na(Co, Cu)₂O₄ and (Ba, Sr)PbO₃. *J. Ceram. Soc. Japan* **2002**, *110*, 727–730. [[CrossRef](#)]
27. Kao, W.; Haberichter, S.L.; Bullock, K.R. Corrosion Resistant Coating for a Positive Lead/Acid Battery Electrode. *J. Electrochem. Soc.* **1992**, *139*, L105–L107. [[CrossRef](#)]
28. Shannon, R.D. Unit Cell and Space Group of SrPbO₃. *J. Solid State Chem.* **1971**, *3*, 184–185. [[CrossRef](#)]
29. Keller, H.L.; Meier, K.H.; Müller-Buschbaum, H. Zur Kristallstruktur von SrPbO₃. *Zeitschrift für Naturforsch.-Sect. B J. Chem. Sci.* **1975**, *30*, 277–278. [[CrossRef](#)]
30. Ritter, H.; Ihringer, J.; Maichle, J.K.; Prandl, W.; Hoser, A.; Hewat, A.W. The Crystal Structure of the Prototypic Ceramic Superconductor BaPbO₃: An X-ray and Neutron Diffraction Study. *Z. Für Phys. B Condens. Matter.* **1989**, *75*, 297–302. [[CrossRef](#)]
31. Shuvaeva, E.T.; Fesenko, E. Synthesis And X-ray Investigation of Perovskites BaPbO₃ and SrPbO₃-Sov. *Phys. Crystallogr.* **1970**, *15*, 321.
32. Hester, J.R.; Howard, C.J.; Kennedy, B.J.; Macquart, R. High-Temperature Structural Studies of SrPbO₃ and BaPbO₃. *Aust. J. Chem.* **2002**, *55*, 543–545. [[CrossRef](#)]
33. Lobanov, M.V.; Kopnin, E.M.; Xenikos, D.; Grippa, A.J.; Antipov, E.V.; Capponi, J.J.; Marezio, M.; Julien, J.P.; Tholence, J.L. Synthesis and Resistivity Properties of Sr_{1-x}LaxPbO_{3-δ} and SrPb_{1-x}BixO_{3-δ}. *Mater. Res. Bull.* **1997**, *32*, 983–992. [[CrossRef](#)]
34. Fu, W.T.; Ijdo, D.J.W. A Comparative Study on the Structure of APbO₃ (A = Ba,Sr). *Solid State Commun.* **1995**, *95*, 581–585. [[CrossRef](#)]
35. Itoh, M.; Sawada, T.; Kim, I.S.; Inaguma, Y.; Nakamura, T. Composition Dependence of Carrier Concentration and Conductivity in (Ba_{1-x}Sr_x)PbO_{3-δ} System. *Solid State Commun.* **1992**, *83*, 33–36. [[CrossRef](#)]
36. Murayama, N.; Yasukawa, M. High Temperature Thermoelectric Properties of Ba_{1-x}Sr_xPbO₃ (0 ≤ x ≤ 1.0). In Proceedings of the Seventeenth International Conference on Thermoelectrics, Proceedings ICT98, Nagoya, Japan, 28 May 1988; IEEE: New York, NY, USA, 1988; pp. 563–566.
37. Keester, K.L.; White, W.B. Crystal Chemistry and Properties of Phases in the System SrO-PbO-O. *J. Solid State Chem.* **1970**, *2*, 68–73. [[CrossRef](#)]
38. Thornton, G.; Jacobson, A.J. A Powder Neutron Diffraction Determination of the Structure of BaPbO₃ at 4.2 K. *Mater. Res. Bull.* **1976**, *11*, 837–841. [[CrossRef](#)]
39. Moussa, S.M.; Kennedy, B.J.; Vogt, T. Structural Variants in ABO₃ Type Perovskite Oxides. On the Structure of BaPbO₃. *Solid State Commun.* **2001**, *119*, 549–552. [[CrossRef](#)]
40. He, J.; Li, T.; Liu, X.; Su, H.; Ku, Z.; Zhong, J.; Huang, F.; Peng, Y.; Cheng, Y.B. Influence of Phase Transition on Stability of Perovskite Solar Cells under Thermal Cycling Conditions. *Sol. Energy* **2019**, *188*, 312–317. [[CrossRef](#)]
41. Tao, S.; Irvine, J.T.S. Discovery and Characterization of Novel Oxide Anodes for Solid Oxide Fuel Cells. *Chem. Rec.* **2004**, *4*, 83–95. [[CrossRef](#)]
42. Ksepko, E.; Winiarski, A.; Ratuszna, A. X-ray Powder Diffraction Study of Structural Phase Transitions in (Ba_{0.5}Sr_{0.5})PbO₃ Perovskite. *Phase Transit.* **2004**, *77*, 335–344. [[CrossRef](#)]
43. Shao, D.; Hutchinson, E.J.; Heidbrink, J.; Pan, W.P.; Chou, C.L. Behavior of Sulfur during Coal Pyrolysis. *J. Anal. Appl. Pyrolysis* **1994**, *30*, 91–100. [[CrossRef](#)]
44. Woodward, P.M. Octahedral Tilting in Perovskites. I. Geometrical Considerations. *Acta Crystallogr. Sect. B Struct. Sci.* **1997**, *53*, 32–43. [[CrossRef](#)]
45. Jorda, J.L.; Lebbou, K.; Galez, P.; Abraham, R. Solid State Equilibrium in the Doubly Substituted (TI, Pb)(Sr, Ba)O₃ System. *J. Alloys Compd.* **1997**, *256*, 34–39. [[CrossRef](#)]
46. Azuma, T.; Sakamoto, Y.; Takahashi, S.; Kuwabara, M. Preparation of Dense BaPbO₃ Ceramic Electrode Materials for Ferroelectric Thin Films and Their Electrical and Thermal Properties. *J. Ceram. Soc. Japan* **1994**, *102*, 2369–2380. [[CrossRef](#)]
47. Hadjarab, B.; Saadi, S.; Bouguelia, A.; Trari, M. Physical Properties and Photoelectrochemical Characterization of SrPbO₃. *Phys. Status Solidi* **2007**, *204*, 2369–2380. [[CrossRef](#)]

Disclaimer/Publisher’s Note: The statements, opinions and data contained in all publications are solely those of the individual author(s) and contributor(s) and not of MDPI and/or the editor(s). MDPI and/or the editor(s) disclaim responsibility for any injury to people or property resulting from any ideas, methods, instructions or products referred to in the content.